Multiplexed volumetric CLEM enabled by antibody derivatives provides new insights into the cytology of the mouse cerebellar cortex

Xiaomeng Han[1], Xiaotang Lu[1], Peter H. Li[2], Shuohong Wang[1], Richard Schalek[1], Yaron Meirovitch[1], Zudi Lin[5], Jason Adhinarta[4], Daniel Berger[1], Yuelong Wu[1], Tao Fang[6], Elif Sevde Meral[7], Shadnan Asraf[8], Hidde Ploegh[6], Hanspeter Pfister[5], Donglai Wei[4], Viren Jain[2], James S. Trimmer[3], Jeff W. Lichtman[1*]

[1] Department of Molecular and Cellular Biology, Harvard University, Cambridge, MA

[2] Google Research, Mountain View, CA

[3] Department of Physiology and Membrane Biology, University of California Davis School of Medicine, Davis, CA

[4] Computer Science Department, Boston College, Chestnut Hill, MA

[5] School of Engineering and Applied Sciences, Harvard University, Cambridge, MA

[6] Program of Cellular and Molecular Medicine, Boston Children's Hospital, Boston, MA

[7] Bezmialem Vakif University School of Medicine, Istanbul, Turkey

[8] School of Public Health, University of Massachusetts Amherst, Amherst, MA

[*] Corresponding Author: jeff@mcb.harvard.edu

Abstract

Mapping neuronal networks that underlie behavior has become a central focus in neuroscience. While serial section electron microscopy (ssEM) can reveal the fine structure of neuronal networks (connectomics), it does not provide the molecular information that helps identify cell types or their functional properties. Volumetric correlated light and electron microscopy (vCLEM) combines ssEM and volumetric fluorescence microscopy to incorporate molecular labeling into ssEM datasets. We developed an approach that uses small fluorescent single-chain variable fragment (scFv) immuno-probes to perform multiplexed detergent-free immuno-labeling and serial electron microscopy on the same samples. We generated eight such fluorescent scFvs that targeted useful markers for brain studies (GFP, GFAP, calbindin, parvalbumin, Kv1.2, VGluT1, PSD-95, and neuropeptide Y). To test the vCLEM approach, six different fluorescent probes were imaged in a sample of the cortex of a cerebellar lobule (Crus 1), using confocal microscopy with linear unmixing, followed by ssEM imaging of the same sample. The results show excellent ultrastructure and superimposition of the different fluorescence channels. We document a poorly described cell type in the cerebellum, two types of mossy fiber terminals, and the subcellular localization of ion channels. Because scFvs can be derived from existing monoclonal antibodies, hundreds of such probes can be generated to enable a wide range of connectomic studies.

Introduction

Mapping neuronal networks that underlie behavior is a central focus in neuroscience. Techniques that reveal the structure and molecular components of neurons and their connections have expanded over the last several decades. Automated high resolution serial section electron microscopy (ssEM) provides detailed structural information about neuronal networks but omits other important features of neuronal ensembles. For example, the molecular markers of cell or synapse types, the localization of specific molecules related to neuronal physiology, or the functional properties of neural circuits cannot be provided by ssEM alone. Therefore, knowledge gained from neuronal networks mapped by ssEM is still limited. There is a need for new technology to incorporate molecular and functional information into ssEM.

Several techniques that are useful for obtaining both structural context and molecular information in the same sample use light and electron microscopy. For light microscopy (LM), methods to colorize cells, such as Brainbow, take advantage of combinatorically expressed fluorescent proteins to enable dense labeling of neurons with multiple, distinct colors (Cai et al., 2013; Livet et al., 2007). However, the resolution of fluorescence imaging is limited by diffraction. This makes it challenging to differentiate among densely packed neurites or to assign the pre- and postsynaptic partners of each synapse. Expansion microscopy (ExM) can overcome this limitation (F. Chen et al., 2015) by physically expanding the dimensions of a sample. When combined with fluorescent lipid labeling (White et al., 2022), ExM has the potential to yield both structural and functional information on neural circuits, but has not yet been used to trace dense neural circuits (Michalska et al., 2022; M'Saad et al., 2022). To label specific molecules, pre- and post-embedding immuno-EM use antibodies tagged with heavy metal particles or enzymes that create electron-dense deposits visible by EM to label specific molecules (Baude et al., 1993; Nusser et al., 1998; Richards et al., 1987). Antibodies conjugated to metal beads of different sizes allow molecular identification of up to three different labels (Nusser et al., 1998). However, pre-embedding immuno-methods require permeabilization to perforate cell membranes, causing them to appear discontinuous in EM images and thus impractical for neural circuit tracing. Post-embedding methods suffer from the loss of antigen epitopes by heavy metal staining. In our experience, many targets are then no longer detectable by immunolabeling. One way to circumvent the permeabilization problem is to transgenically express EM-visible tags like miniSOG (Shu et al., 2011) and APEX (Martell et

al., 2012). These probes circumvent the need for permeabilization to allow antibody penetration of cells. Genetically encoded APEX2 tags can be used to label one or more cell-types with ssEM (Joesch et al., 2016; Zhang et al., 2019), the current maximum number of labels being four (Zhang et al., 2019).

Volumetric correlated light and electron microscopy (vCLEM) are techniques in which fluorescence LM and ssEM are performed on the same sample and subsequently co-registered together. Because multiplex labeling (more than three colors) can easily be achieved by fluorescence LM, for example by spectral unmixing (Seo et al., 2022; Zimmermann et al., 2014), vCLEM can potentially incorporate more molecular and functional information into ssEM datasets. vCLEM performed on animals that have a fluorescent protein or a calcium indicator delivered as transgenes can identify certain cell types (Bishop et al., 2004; Hwang et al., 2021) or show the connectivity patterns of functionally identified cells (Kuan et al., 2022; Lee et al., 2016; Vishwanathan et al., 2017). However, it has been difficult to achieve multiplex labeling using these approaches, because of the difficulty breeding more than three transgenes into a single strain of mice. vCLEM techniques based on immunofluorescence provide an alternative option for multiplex labeling. However, when using conventional antibodies for immunofluorescence, these methods are problematic because they require permeabilizing detergents that compromise membrane structure (Fang et al., 2018). Array tomography circumvents the need for permeabilization by performing immunofluorescence on resin-embedded serial semithin sections, followed by heavy metal staining and EM imaging (Micheva & Smith, 2007), but the ultrastructure is compromised and the sections are too thick for connectomics. Detergent-based permeabilization is also avoided by use of nanobodies as immunolabels (Fang et al., 2018). Nanobodies are single domain immuno-binders derived from camelid heavy chain only antibodies (Ingram et al., 2018) and are only 1/10 the size of conventional antibodies, allowing them to diffuse into tissue samples without permeabilizing agents like Triton X-100. In the presence of preserved extracellular space (ECS), nanobodies diffused over a distance of ~100 micrometers into brain samples within 48 hours of their application (Fang et al., 2018). ECS preservation also facilitates standard antibody (IgG) diffusion into brain tissue samples without detergent treatment (Fulton & Briggman, 2021; Lu et al., 2023). However, neither method achieved more than triple labeling due to limitations of available probe panels. The goal of this study is to develop a larger number of immuno-probes that diffuse across cell membranes in the absence of

detergents and combine them with multiplex imaging techniques like spectral unmixing.

One approach is to generate smaller immuno-probes from full-size IgG monoclonal antibodies. Monoclonal antibodies (mAbs) are homogeneous with respect to their amino acid sequence and the epitope recognized (Harlow, 1988). Creating smaller probes from existing mAbs requires knowledge of a particular mAb's amino acid sequence. These sequences can be obtained by cDNA cloning from the hybridoma cells that produces the mAb (Andrews et al., 2019; Y. Chen et al., 2018; Debs et al., 2012; Trimmer, 2020). Alternatively, the amino acid sequence can be derived from the mAb protein itself, if the hybridoma cells are not available (Bandeira et al., 2008; Sen et al., 2017). With the knowledge of the amino acid sequence of a mAb, it is possible to synthesize a smaller single-chain variable fragment (scFv) that retains the binding specificity of the progenitor mAb. ScFvs are built by recombinantly linking the V_H and V_L domains of mAbs via a flexible peptide linker (Figure 1 a) (Ahmad et al., 2012). Only if the V_H and V_L pair correctly (~60% of the time) do they bind to the antigen (Ahmad et al., 2012; Trimmer, 2020). Because a scFv consists of only V_H and V_L domains, they are 1/5 the size of conventional antibodies. We surmised that their small size would allow them to diffuse into tissue samples without detergent-based permeabilization, as is the case for nanobodies (Fang et al., 2018). Because there exist extensive collections of well-characterized mAbs that selectively label neuronal cell types or signaling molecules (*UC Davis/NIH NeuroMab Facility*, n.d.), it is possible to develop a large collection of the corresponding scFvs for use in the nervous system. Because scFvs are produced recombinantly (Trimmer, 2020), they can be engineered so that different fluorescent dyes can easily be conjugated to them for multiplex imaging.

To test this idea, we developed eight scFvs based on eight well-characterized mAbs and conjugated each scFv with fluorescent dyes (see Table 1). Each scFv in this panel proved effective as a detergent-free immunofluorescent probe. We then used linear unmixing with confocal microscopy to visualize five different functional molecular markers in the same brain sample and co-registered these labels to ssEM volumes with pristine preservation of the ultrastructure of the same samples. Because the volumetric fluorescent and electron microscopy image data were of excellent quality, this approach holds promise for routine linking of molecular information to connectomic information obtained from the same tissue samples.

Results

Generation of scFv-based immuno-probes and their use in detergent-free immunofluorescence

To test the hypothesis that scFvs could work as immuno-probes for detergent-free immunofluorescence, we first generated an anti-GFP scFv based on the amino acid sequence of the anti-GFP mouse mAb N86/38 (*UC Davis/NIH NeuroMab Facility*, n.d.). This mAb binds to both GFP and the GFP derivative YFP. The sequence (derived by PCR cloning from hybridoma cells (Andrews et al., 2019) was used to construct an scFv expression which connected the V_H and the V_L domains via a (GGGGS) x 3 linker (Figure 1 a). A sortase tag (Fang et al., 2018) was added to the C-terminus of the V_L domain of the scFv for dye conjugation, followed by a 6 x His tag for purification. After the scFv was expressed in Expi 293 cells and purified by affinity chromatography, the fluorescent dye 5-TAMRA was installed (see Methods) (Figure 1 a). We tested this red fluorescent anti-GFP scFv probe with our detergent-free immunofluorescence protocol (see Methods) on cerebral cortex from YFP-H mice (Feng et al., 2000) (n=3). The images showed colocalization of fluorescence signals from native YFP and red fluorescence from the scFv probe, with no bleed through (Figure 1 b; Sup. Figure 1 a) The scFv probe thus retains the binding properties of the parental mAb and penetrates aldehyde-fixed brain tissue without the need for detergent treatment. Although the fluorescent signals colocalized in cell bodies and thick dendrites, some thinner neuronal processes were not well labeled (arrows in Figure 1 b), suggesting the need for further optimization. We were also interested to learn the degree to which scFvs can penetrate tissue volume. We attempted to use this probe to immunolabel samples (n=2) from the mouse cerebral cortex, using sections with a thickness of 300 µm and without detergent treatment (see Methods). After a free-floating incubation of seven days, this scFv penetrated to a depth of ~60 µm into the tissue (Sup. Figure 1 b). This was much deeper than the penetration of a fluorescently labeled anti-GFP polyclonal antibody (pAb) which only penetrated to a depth of ~10 µm into the sample (Sup. Figure 1 b). Furthermore, the use of an ECS preserving perfusion protocol (Lu et al., 2023) improved penetration by the scFv to a depth of >100 µm (Sup. Figure 1 c). Fluorescently labeled nanobodies, which are about half the size of scFvs, penetrate even deeper (Sup. Figure 1 b, c).

Table 1. Fluorescent scFv immuno-probes generated in this work.

Target	mAb Clone No.	Fluorescent dyes conjugated
GFP	N86/38	5-TAMRA
Calbindin	L109/57	5-TAMRA, Alexa Fluor 488
GFAP	N206B/9	5-TAMRA
VGluT1	N28/9	5-TAMRA, Alexa Fluor 532
PSD-95	K28/43	5-TAMRA
Kv1.2	K14/16	Alexa Fluor 594
Parvalbumin	L114/81	Alexa Fluor 647
Neuropeptide Y	L115/13	Alexa Fluor 647

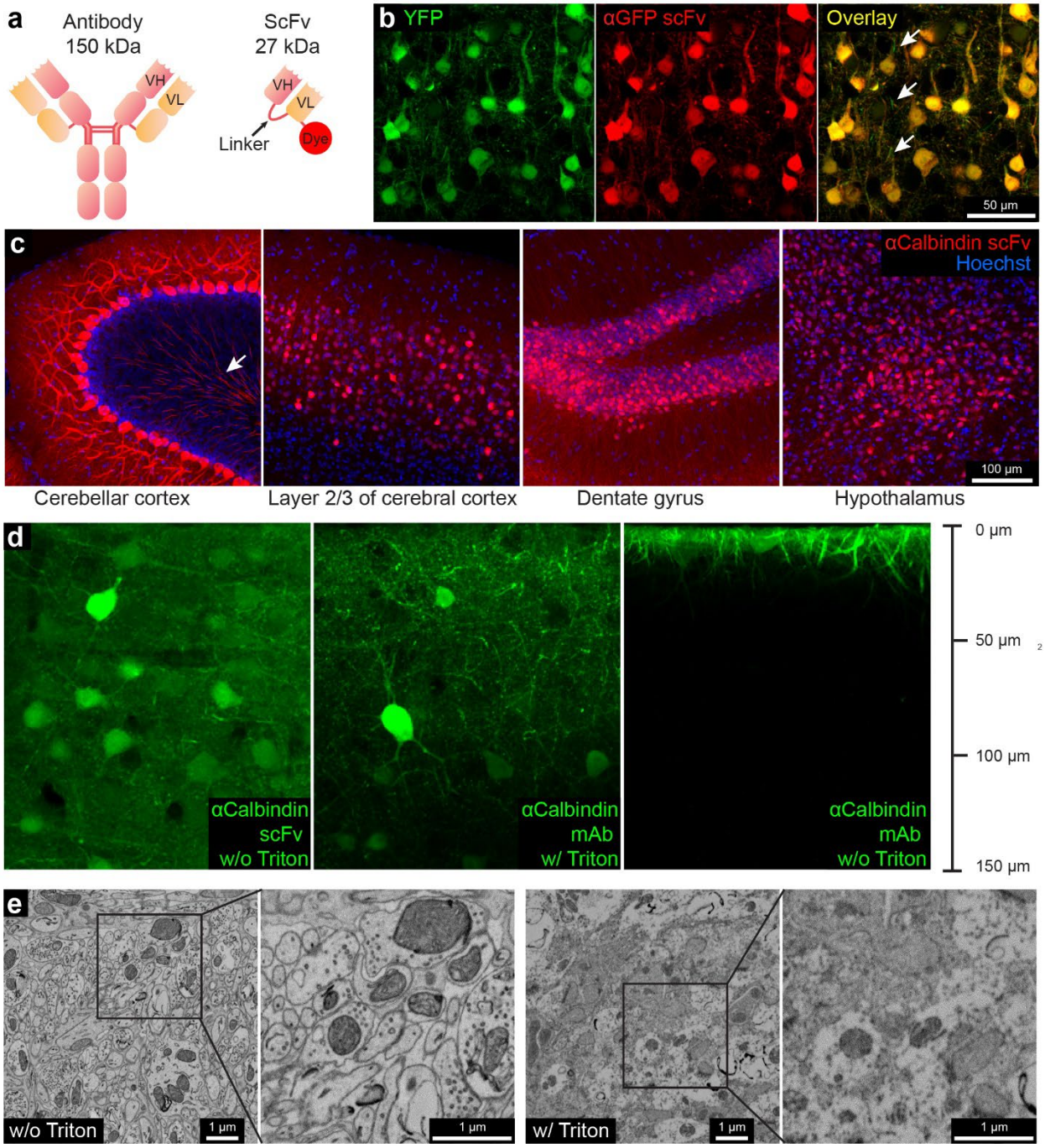

Figure 1. Fluorescent scFv probes label brain tissues without detergents to preserve electron microscopy ultrastructure.

a, Schematic representations of a full-length IgG antibody and an scFv probe with a conjugated fluorescent dye. **b**, Confocal images from the cerebral cortex of a YFP-H mouse labeled using a GFP-specific scFv probe conjugated with the red dye 5-TAMRA. Arrows show thinner neuronal processes, perhaps myelinated, that are not labeled by scFv. **c**, Brain regions labeled with a calbindin-specific scFv probe conjugated with 5-TAMRA. The arrow in the left panel shows myelinated Purkinje cell axons in the granule layer. **d**, Tissue penetration depth comparison of scFvs, mAbs, and the role of detergents in

improving the depth of labeling. **e**, Comparison of ultrastructure with and without Triton X-100 on scFv labeled samples. Boxed insets are shown at higher magnification in adjacent panels.

We then proceeded to produce an scFv probe for an endogenously expressed protein (calbindin, also known at calbindin-D 28k). This probe was based on the well-characterized mouse mAb L109/57 (*UC Davis/NIH NeuroMab Facility*, n.d.). Calbindin is a calcium-binding protein expressed by certain neuronal types in various brain regions, such as cerebellar Purkinje cells, neurons in layer 2/3 of the cerebral cortex, dentate gyrus granule cells, as well as a subpopulation of hypothalamic neurons (Andressen et al., 1993). Because previous studies showed that an scFv's performance improved as the length of linker increased (X. Chen et al., 2013; Yusakul et al., 2016) we chose a (GGGGS) x 4 linker rather than a x 3 linker. We conjugated this scFv to fluorescent dyes and tested it on brain tissue samples (n=2) from wild type C57BL/6J mice with our detergent-free immunofluorescence protocol. This scFv probe labels neurons in all four brain regions where calbindin-expressing neurons are highly abundant (Figure 1 c). Thus, scFv probes can label endogenous protein targets via detergent-free immunofluorescence. The anti-calbindin scFv labels many neuronal processes in the cerebellar granule layer (arrow in Figure 1 c, first panel). Presumably these are the myelinated axons of Purkinje cells. The stronger labeling of cellular processes, obtained with this scFv when compared to the anti-GFP scFv, may be explained by the different lengths of the linkers used. We repeated the penetration test (n=2) (see Methods) for this probe and found that the anti-calbindin scFv can penetrate to a depth of ~150 μm in a 300-μm tissue slice, a distance beyond the maximum imaging depth of confocal microscopy without tissue clearing (Figure 1 d, first panel). This is the same penetration depth as seen for the L109/57 mAb from which the scFv is derived when using a conventional immunofluorescence protocol (*Immunofluorescence Labeling of Free-Floating Perfusion-Fixed Brain Sections*, 2016), with Triton X-100 as the detergent for permeabilization (Figure 1 d, the first and second panels). In stark contrast, the mAb only penetrates the surface of a tissue sample prepared without detergent (Figure 1 d, the third panel). The improved binding afforded by the use of a longer linker may have given rise to observable signals deeper in the specimen when compared to the anti-GFP scFv.

We continued to explore whether our detergent-free immunofluorescence protocol preserves fine ultrastructure. We performed a routine EM staining protocol (see Methods) on a 120-μm thick cerebellar

cortex sample that had been treated for 7-days according to a free-floating immunofluorescence protocol both with and without the use of Triton X-100 for membrane permeabilization (see Methods). The ultrastructure of the sample without Triton X-100 was well-preserved, with continuous membrane structures and clearly visible synaptic vesicles (Figure 1 e, the first and second panels). In contrast, treatment of samples with Triton X-100 generated EM images in which membrane structures were discontinuous and synaptic vesicles no longer identifiable (Figure 1 e, the third and fourth panels).

Generation of fluorescent scFv probes targeting various targets

To achieve multiplex labeling with scFvs, we included six additional scFvs (anti-VGluT1, anti-GFAP, anti-Kv1.2, anti-parvalbumin, anti-PSD-95, and anti-neuropeptide Y) with the anti-GFP and anti-calbindin probes. These scFvs are based on six well-characterized mouse mAbs (*UC Davis/NIH NeuroMab Facility*, n.d.) (see Table 1). We conjugated them with various fluorescent dyes via the sortase reaction to create fluorescent immuno-probes (see Table 1). We then validated them by comparing scFv versus parental mAb immunofluorescence for each probe (Sup. Figures 2-4). Probes for calbindin (CB), VGluT1, GFAP, Kv1.2, and parvalbumin (PV) generated detergent-free immunofluorescence patterns that were similar to or better than their parental mAbs in Crus 1 of the cerebellar cortex (Figure 2 a; Sup. Figure 2; Sup. Figure 3). The scFvs that target CB and PV produced more consistent labeling results for the cell bodies and nuclei of Purkinje cells than labeling with full-size mAbs, which never labeled the nuclei of Purkinje cells (Sup. Figure 2 a, e). Nonetheless, nuclear labeling varied between cells (Sup. Figure 2 a, e). We think this variability is attributable to variable expression levels of the CB and PV targets, as shown for Purkinje cells in different lobules (Brandenburg et al., 2021; Celio, 1990). Levels of CB and PV are variable in both the cell nucleus and cytoplasm of Purkinje cells (German et al., 1997; Schmidt et al., 2007). The axons of Purkinje cells were well labeled with both anti-CB and anti-PV scFvs (Sup. Figure 2 a, e; Sup. Figure 3), unlike labeling seen with full size antibodies. This difference is likely a consequence of impaired access of full-size antibodies to myelinated axons. Post-embedding labeling and thin cryosections have shown that both PV and CB are expressed in axons (Kim et al., 2009; Kosaka et al., 1993), confirming the results shown here with scFvs. Probes for PSD-95 and neuropeptide Y (NPY) showed results similar to those found with full size mAbs (Sup. Figure 4), but only when labeling was

done on tissue samples where the ECS was preserved (Lu et al., 2023).

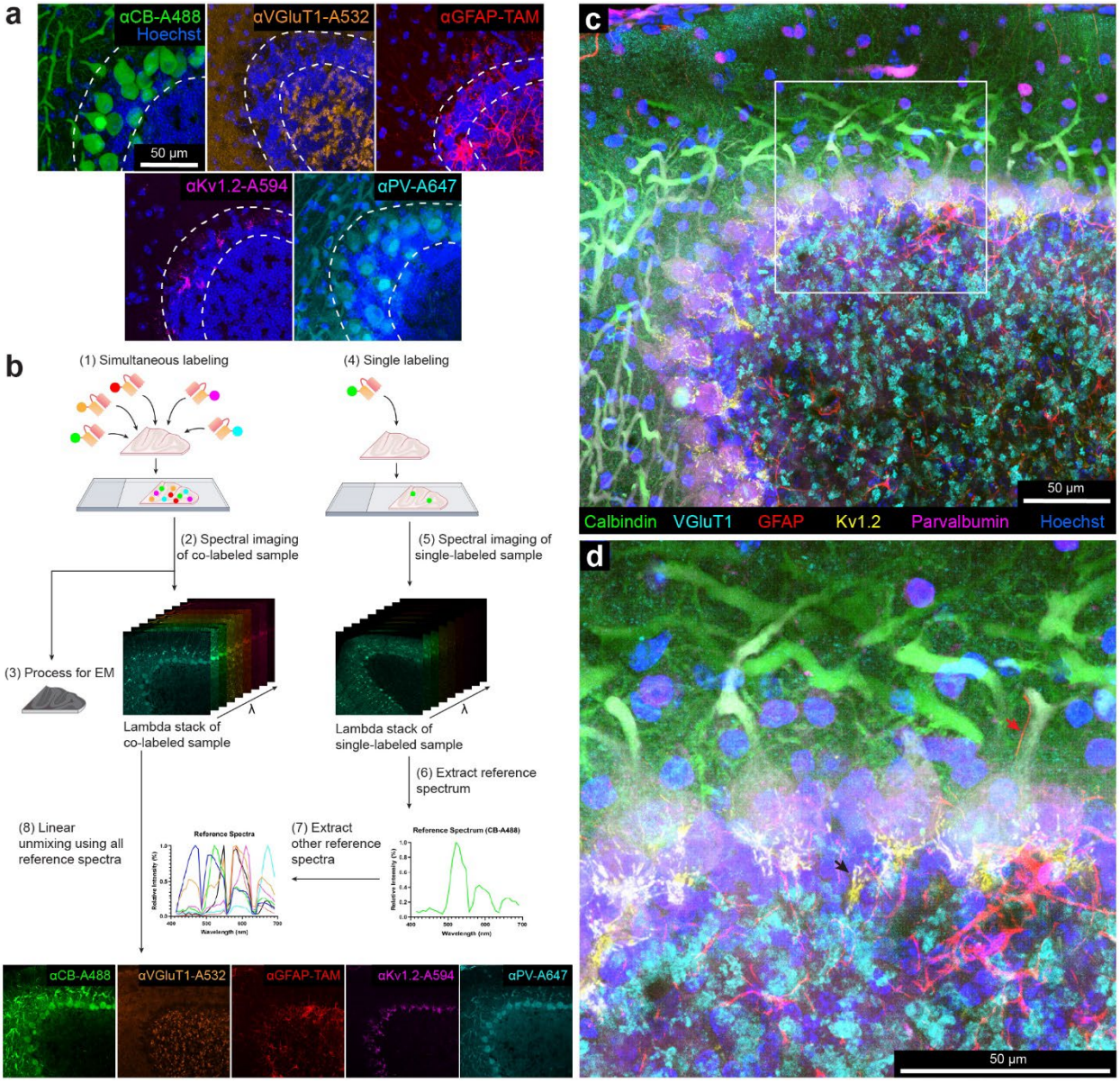

Figure 2. Multi-color immunofluorescence enabled by scFv probes and linear unmixing of confocal micrographs.

a, Confocal images of different sections from the cerebellum labeled with: a calbindin-specific scFv probe conjugated with Alexa Fluor 488, a VGluT1-specific scFv probe conjugated with Alexa Fluor 532, a GFAP-specific scFv probe conjugated with 5-TAMRA, a Kv1.2-specific scFv probe conjugated with Alexa Fluor 594, and a parvalbumin-specific scFv probe conjugated with Alexa Fluor 647. The double dotted lines delineate the Purkinje cell layer. (see Sup. Figure 2 for larger fields of view). CB, calbindin; VGluT1, vesicular glutamate transporter 1; GFAP, glial fibrillary acidic protein; Kv1.2, voltage-gated potassium

channel subfamily A member 2; PV, parvalbumin; TAM, 5-TAMRA. **b**, Workflow of multi-color imaging enabled by scFv probes and linear unmixing (see text). **c**, Maximum intensity projection of the multi-color fluorescence image stack acquired by linear unmixing of confocal images. The signal of each fluorescent dye was pseudo-colored for better visualization. **d**, Enlarged boxed inset from **c**. Red arrow indicates a Bergmann fiber (GFAP-positive) adjacent to the main dendrite of a Purkinje cell. Black arrow indicates sites where axons form a pinceau structure labeled by the Kv1.2-specific scFv probe.

Multiplexed vCLEM based on scFv-enabled immunofluorescence using linear unmixing

To perform multiplexed vCLEM, we chose five fluorescent probes with different targets and different fluorophores (anti-CB-Alexa Fluor 488, anti-VGluT1-Alexa Fluor 532, anti-GFAP-5-TAMRA, anti-Kv1.2-Alexa Fluor 594, and anti-PV-Alexa Fluor 647) to simultaneously label a sample with the thickness of 120 µm from Crus 1 (Figure 2 b, see Methods). Because these fluorophores have overlapping excitation and emission spectra (Sup. Figure 5), we used linear unmixing on a laser-scanning confocal microscope for multiplex imaging. A lambda stack of the multicolor sample with a depth of 52 µm was imaged by confocal microscopy (Zeiss LSM 880) using a spectral detector (Figure 2 b; Sup. Figure 5 b). Because a fluorophore's reference spectrum (required for linear unmixing) may vary depending on brain regions (Seo et al., 2022) we acquired a lambda stack for each fluorophore in individually labeled samples from the same region as the multi-labeled sample (Figure 2 b; Sup. Figure 5 c). Using a linear unmixing algorithm and the reference spectra of all five dyes (Figure 2 b; Sup. Figure 5 c), the lambda stack of the multi-labeled sample was separated into five fluorescent probe channels (Figure 2 b; Sup. Figure 6 a). Linear unmixing can be accomplished more efficiently by extracting reference spectra from the multi-labeled sample in several different ways (Lelouard et al., n.d.). Unfortunately, these approaches did not give satisfactory results with this sample (Sup. Figure 6 b, c).

The spectrally unmixed labeling pattern for each probe was distinct and resembled what we found in the individually labeled samples (Figure 2 c; Sup. Figure 6 a; Sup. Figure 7). In the sample described above, the Hoechst channel (labeling cell nuclei) was acquired separately, with a single 405-nm laser for excitation, because the short excitation and emission wavelength of Hoechst scattered strongly and lost intensity dramatically with depth. This scatter required a 10-fold increase in laser power for the deepest parts of the volume. To determine if this separate imaging regimen was necessary, in a separate but identically prepared sample we combined the weaker Hoechst channel with the other linear unmixing channels (see Methods). The unmixing result was equally good (Sup. Figure 8), although more difficult to

obtain, indicating that it was not necessary to image Hoechst separately. Overall, we used linear unmixing to acquire a multi-color fluorescence image volume (304 µm x 304 µm x 52 µm), showing the labeling of the five scFv probes (Figure 2 c, d; Sup. Figure 9). Each fluorescence channel is highly specific for the labeling pattern of the corresponding scFv. For example, the labeling of Bergmann fibers (red arrow) by the anti-GFAP scFv and the labeling of the axons in pinceau structures (black arrows) by the anti-Kv1.2 scFv are easily distinguishable (Figure 2 d). After imaging on the confocal microscope was completed, the sample was stained with heavy metals and embedded in resin (see Methods).

After the sample was embedded in resin, an isotropic resolution (voxel size 1.15 μm^3) volume of the sample was acquired by µCT (see Methods). The sample was then cut into ~4000 serial sections of 30 nm thickness using an automated tape-collecting ultramicrotome (ATUM). The serial sections were collected onto carbon-coated Kapton tape, which was cut into strips and affixed onto silicon wafers for EM imaging. We used a single-beam scanning electron microscope to collect a low-resolution overview image subvolume of 1 mm x 1 mm x 60 µm with a voxel size of 150 nm x 150 nm x 1.35 µm, which came from the more superficial half of all the serial sections where confocal imaging was of high quality. We then used a multi-beam scanning electron microscope to collect a high-resolution volume of 164 µm x 200 µm x 26 µm at a resolution of 4 nm x 4 nm x 30 nm (Figure 3 a), comprising the most superficial 22% of the serial sections. Tissue ultrastructure appeared well preserved throughout the 60-µm subvolume that included all layers of the cerebellar cortex (Figure 3 a, 1-4; Sup. Figure 10).

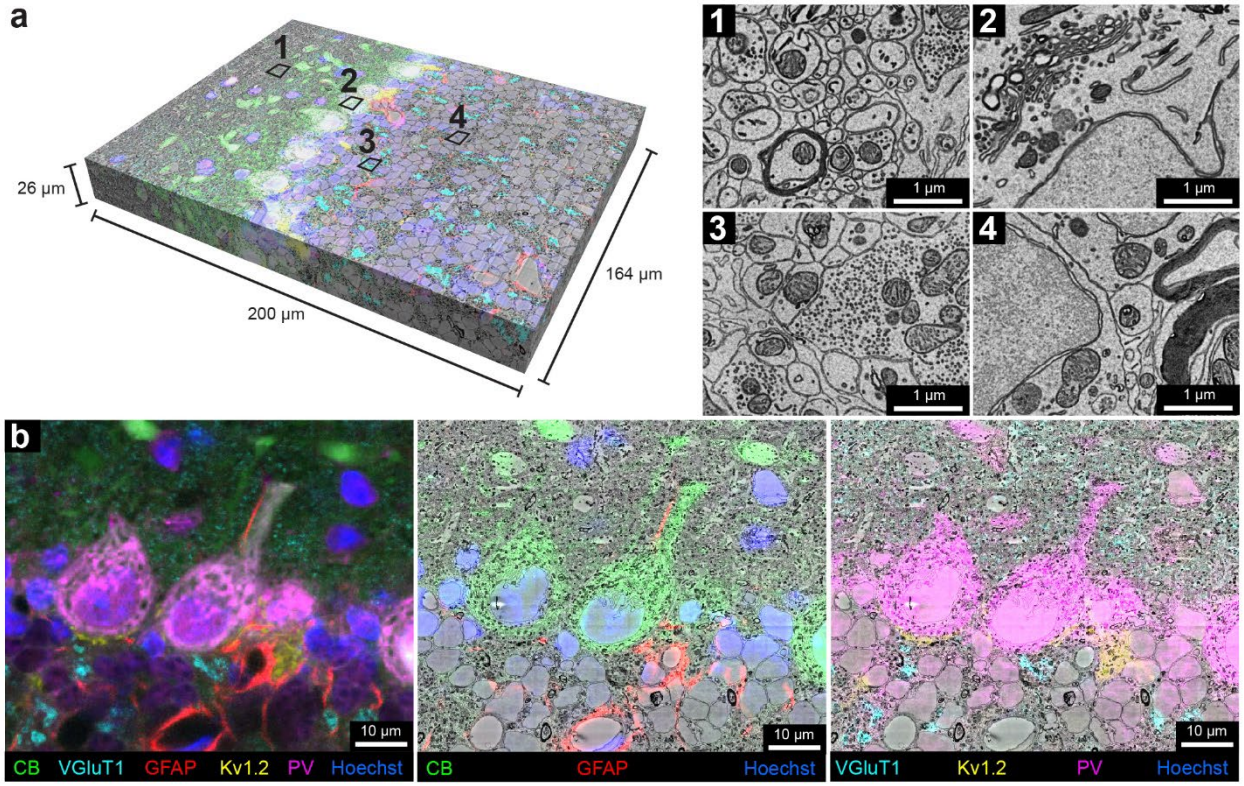

Figure 3. Multi-color volumetric CLEM enabled by scFv-assisted immunofluorescence.

a, The high-resolution ssEM volume acquired from the cerebellar lobule, Crus 1 with multi-color immunofluorescence from scFv probes separated by linear unmixing. The multi-color fluorescence data was co-registered with the high-resolution ssEM data. Numbers **1**-**4** indicate approximate regions where the ultrastructure was examined at high resolution. Owing to the absence of detergent in immunofluorescence labeling, fine ultrastructure was preserved throughout the ssEM volume, such as in the molecular layer (**1**), in the Purkinje cell layer (**2**), in the glomeruli in the granule cell layer (**3**), and in the granule cell bodies (**4**). **b**, Demonstration of the overlay between fluorescence signals and EM ultrastructure. Left panel shows the multi-color six-channel fluorescent image of slice 250 (of 848) of the spatially transformed fluorescence image volume. Middle panel shows three fluorescence channels corresponding to the labeling of CB, GFAP, and Hoechst overlaid onto the EM micrograph of slice 250. Right panel shows four fluorescent channels corresponding to the labeling of VGluT1, Kv1.2, PV, and Hoechst overlaid onto the EM micrograph of slice 250.

Co-registration between the stacks of fluorescence images and EM volumes is challenging because of the various ways by which samples can be distorted by the two imaging modalities. These include rotation, tilt, stretch, and warping (Begemann & Galic, 2016). We developed a workflow to mitigate these challenges by visually finding common fiduciaries (such as blood vessels) in the µCT volume and confocal volume as an intermediate step to guide the trimming of the block to the relevant region prior to ultra-thin sectioning (see Methods). To target the high-resolution EM imaging, we next

registered the confocal stack to the low-resolution EM stack. For the final, high-precision co-registration between the six-color fluorescence confocal volume and the high-resolution EM volume, 188 manually picked landmark points that corresponded to the same sites in the two volumes were placed on blood vessels, cell nuclei, cell bodies, and axons (Sup. Figure 11). A 3D transformation of the fluorescence volume was produced by a thin plate spline interpolation based on the point correspondences (BigWarp in FIJI) (Bogovic et al., 2016). The transformed fluorescence volume was then overlaid with the high-resolution EM volume to create the vCLEM dataset (Figure 3 a). In any slice of this dataset, the fluorescence signals from the molecular markers corresponded with EM ultrastructure (Figure 3 b; Sup. Figure 12). Figure 3 b shows an example slice in which calbindin (green) correlates with Purkinje cells and their dendrites, GFAP (red) with astrocytes around blood vessels, VGluT1 (cyan) with parallel fiber boutons in the molecular layer as well as mossy fiber terminals in the granule layer, Kv1.2 (yellow) with pinceau surrounding Purkinje cell axons, and parvalbumin (magenta) with both Purkinje cells and molecular interneurons.

In order to facilitate visualization of the vCLEM dataset, we imported it into Neuroglancer (*Neuroglancer Documentation*, n.d.) where each fluorescence channel and the EM channel can be visualized separately or simultaneously, and navigation through slices and different resolution levels can be carried out easily.

3D reconstruction of cells and subcellular structures identified by scFv labeling in the cerebellar cortex

An important question is whether the EM data, with six-color immunolabeling superimposed, is of sufficient quality to be successfully segmented by automatic means. Two different methods of automatic segmentation were successful. We used a flood-filling network (Januszewski et al., 2018) pretrained on a different dataset (Shapson-Coe et al., 2021) at either 32 nm or 16 nm and without any new ground truth (Sup. Figure13 a, b). We also used another method developed in our lab (Meirovitch et al., 2018; Pavarino et al., 2023) to generate high-quality 2D membrane predictions, as well as 2D segmentation at 8 nm resolution (Sup. Figure13 c, d) following several rounds of training with manually generated ground truth. The success of the automatic segmentation indicates that the ultrastructure is not compromised by

the detergent-free scFv immunofluorescence labeling protocol.

We then analyzed the CLEM data by reconstructing the EM ultrastructure (see Methods) at sites labeled with each of the five molecular markers (calbindin, GFAP, parvalbumin, Kv1.2, and VGluT1).

Calbindin (CB): In the cerebellar cortex, calbindin is expressed by Purkinje cells and some Golgi cells in the granule layer (Celio, 1990; Garcia-Segura et al., 1984; Scotti & Nitsch, 1992). In the vCLEM dataset, labeling of the anti-calbindin scFv (green fluorescence signal in Figure 4 a; Sup. Figure 14) corresponded to Purkinje cell bodies (Figure 4 a, b), a few likely large Golgi cells in the upper granule cell layer (Palay & Chan-Palay, 2012) (Sup. Figure 14 b, c), and heavily myelinated axons that presumably arose from Purkinje cells (Sup. Figure 14 a, inset 2). 3D reconstructions of one of the labeled Purkinje cells (Figure 4 c; Sup. Figure 14 a) and one of the labeled Golgi cells (Sup. Figure 14 d) showed that their morphologies were similar to previous Golgi/ultrastructural studies of rat cerebellum (Palay & Chan-Palay, 2012). The synaptic inputs from parallel fibers onto Purkinje cells are also obvious (Figure 4 c, d). In addition, we found that the dendritic trees of Purkinje cells in this region (Crus I) were not perpendicular to the rostral-caudal axis but intersected at the axis at an angle of around 55° (Sup. Figure 14 a, inset 1).

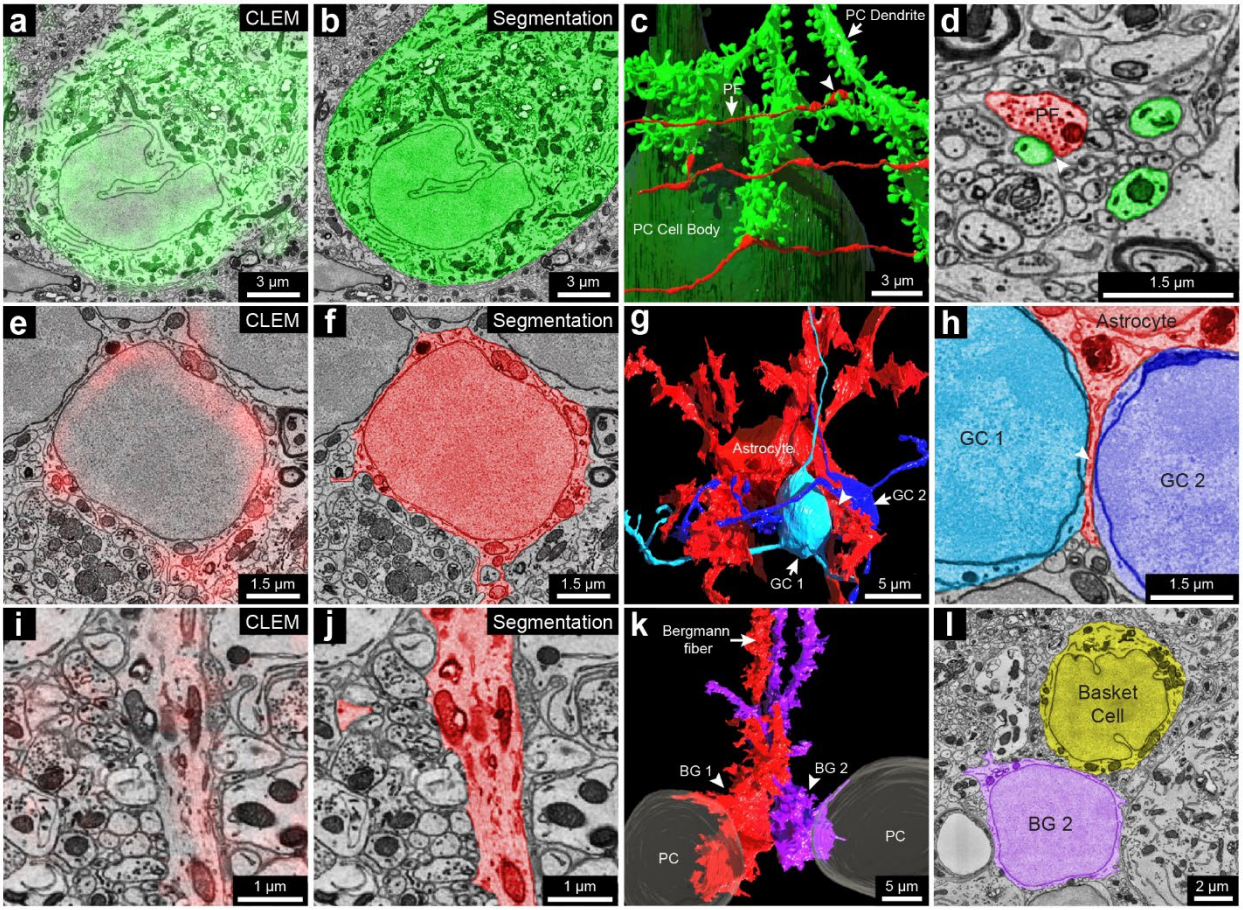

Figure 4. 3D reconstruction of cells labeled by the calbindin-specific and the GFAP-specific scFv probes.

a, 2D CLEM image showing the fluorescence signal (green) of the calbindin-specific scFv probe overlaps with the cell body of a Purkinje cell. **b**, EM image showing the 2D segmentation (green) of the calbindin positive Purkinje cell based on labeling shown in **a**. **c**, 3D reconstruction of the Purkinje cell labeled in **a**. The cell body is labeled in dark green. A dendritic branch is labeled in light green. Three parallel fibers are shown that made three synapses onto three spine heads of the dendritic branch. Arrowhead, a synapse made by a parallel fiber onto a spine head. PC, Purkinje cell; PF, parallel fiber. **d**, EM image showing the 2D segmentation of the synapse labeled by the arrowhead in **c** between a parallel fiber (red) and a spine head of the dendritic branch (green). **e**, 2D CLEM image showing the fluorescence signals (red) of the GFAP-specific scFv probe overlaps with the cell body of a velate astrocyte in the granule cell layer. **f**, EM image showing the 2D segmentation (red) of the cell body of the velate astrocyte in **e**. **g**, 3D reconstruction of the velate astrocyte (red) labeled in **e** and two nearby granule cells (light and dark blue). The velate astrocyte extended a veil-like glial process (arrowhead) between the two granule cells. GC, granule cell. **h**, EM image showing the 2D segmentation of the veil-like glial process (arrowhead) between the cell bodies of two granule cells. **i**, 2D CLEM image showing the fluorescence signals (red) of the GFAP-specific scFv probe overlaps with a Bergmann fiber. **j**, EM image showing the 2D segmentation (red) of the Bergmann fiber labeled in **i**. **k**, 3D reconstruction of two Bergmann glial cells (BG1 and BG2) traced back from their Bergmann fibers labeled by the GFAP-specific scFv probe (e.g. in **i**). BG, Bergmann glial cell. **l**, EM image showing the 2D segmentation of the cell body of BG2 and a nearby basket cell. Note the lack of infoldings in BG2's nuclear membrane compared to the basket cell.

GFAP: This protein is expressed by astrocytes and Bergmann glial cells whose cell bodies reside in the Purkinje layer and whose processes (also known as Bergmann fibers) extend into the molecular layer (Bignami & Dahl, 1973; Bignami et al., 1972). As expected, labeling seen with the anti-GFAP scFv (red fluorescence signal in Figure 4 e, i) corresponded to the cell bodies and processes of granule layer astrocytes (Figure 4 e, f) and the vertical Bergmann fibers in the molecular layer (Figure 4 i, j). Although the cell bodies of granule layer astrocytes have a similar appearance to those of granule cells in EM micrographs (Figure 4 f; Sup. Figure 15 a, insets 1,2), 3D reconstruction of one of the labeled cells shows the typical morphology of a velate astrocyte (Palay & Chan-Palay, 2012) that is different from the structure of nearby granule cells, despite their similar cell body ultrastructure (Figure 4 g; Sup. Figure 15 a). The reconstructed velate astrocyte extended a thin, veil-like glial process between two granule cells (Figure 4 g, h). GFAP labeling was also seen in the processes of Bergmann glia but not in their cell bodies (Figure 4 i; Sup. Figure 15 b, insets). Two Bergmann glia cell bodies were found by tracing back from their labeled processes (Figure 4 i; Sup. Figure 15 b). These cell bodies were adjacent and between two Purkinje cells (Figure 4 k; Sup. Figure 15 b). Although they were similar in size to nearby basket cells, they were distinguishable by virtue of the lack of infoldings in their nuclear membranes (Figure 4 l).

Parvalbumin (PV): This protein is expressed by molecular layer interneurons (MLIs), Purkinje cells and Purkinje layer interneurons (Celio, 1990; Kozareva et al., 2022). The labeling we observed (magenta fluorescence signal in Figure 5 a; Sup. Figure 16 a, b) in the molecular layer co-registered with MLIs (Figure 4 b; Sup. Figure 16 c, d) that have in-folded nuclear membranes. Among PV positive MLIs (n = 22) that we partially reconstructed we chose three for full reconstruction. These neurons were located at three different levels of the molecular layer (Figure 4 c) and exhibited different morphologies as has been previously described (Kozareva et al., 2022).

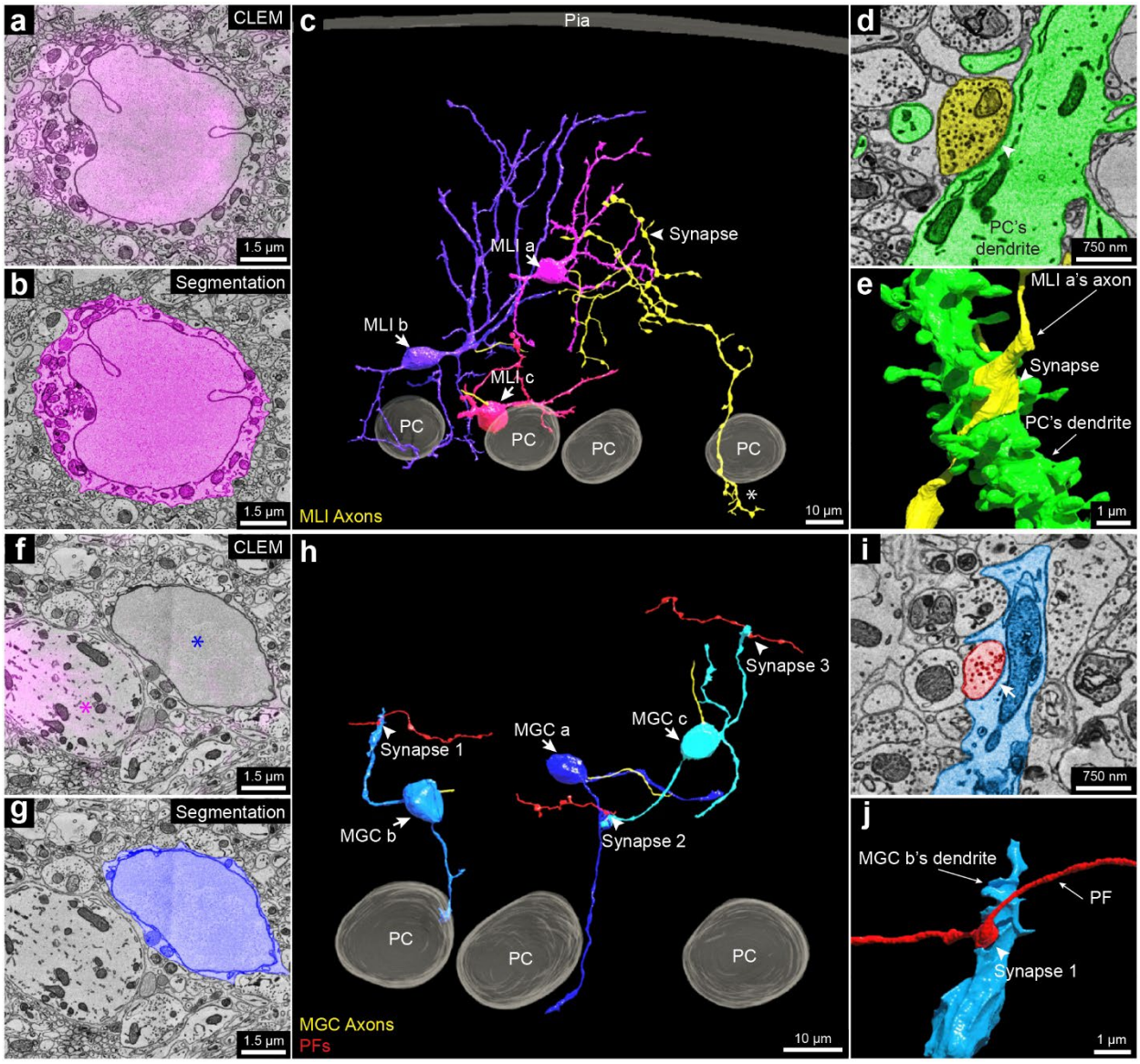

Figure 5. 3D reconstruction of the molecular layer interneurons and granule cells distinguished by PV-specific scFv probes.

a, 2D CLEM image showing the fluorescence signals (magenta) of the parvalbumin-specific scFv probe overlap a cell body of a molecular layer interneuron (MLI, also known as MLI a in **c**). **b**, EM image showing the 2D segmentation (magenta) of the MLI in **a**. **c**, 3D reconstruction MLI a, MLI b, and MLI c, showing their positions relative to the pia and the Purkinje cell layer. Their axons are labeled in yellow. MLI a, the interneuron that is farthest from the Purkinje cell layer axon branched extensively in the volume and innervated a Purkinje cell's dendritic shaft at the arrowhead. This same axon was also part of the pinceau structure that surrounds a different Purkinje cell's axon initial segment (asterisk, also see Sup. Figure 16 e). Based on these features, this interneuron appears to be a deep axon stellate cell (Palay & Chan-Palay, 2012). **d**, EM image showing the 2D segmentation of the synapse labeled by the arrowhead in **c** between MLI a's axon (yellow) and a dendrite of a Purkinje cell (green). Arrowhead points to the location of the synapse. **e**, 3D reconstruction of the synapse labeled by the arrowhead in **d**. **f**, 2D CLEM image showing the fluorescence signal (magenta) of the parvalbumin-specific scFv which overlaps dendrites of a Purkinje cell (magenta asterisk), but does not label a molecular layer granule cell (blue

asterisk). **g**, Same EM image as **f** showing the 2D segmentation (dark blue) of the cell body of a molecular layer granule cell (MGC). **h,** 3D reconstructions of MGC a, MGC b, and MGC c, with relationship to three Purkinje cells (also shown in the right part of **c**). Unlike granule cells with cell bodies in the granule cell layer, these MGCs received synapses from parallel fibers. Three such synapses between parallel fibers (red) and the three MGCs are labeled. **i**, EM image showing the 2D segmentation of synapse 1 in **h**. **j**, 3D reconstruction of synapse 1 labeled by the arrowhead in **i**.

The PV-positive labeling allowed examination of a set of neurons in the molecular layer that are PV-negative (Figure 5 f, g; Sup. Figure 16 f, g). All of these neurons (n=7) showed morphological features consistent with them being a rarely studied type of neuron, known as molecular layer granule cells (MGCs) (Berciano & Lafarga, 1988; Lafarga & Berciano, 1985; Palay & Chan-Palay, 2012). MGCs are sometimes regarded as ectopic granule cells that did not migrate to the granule cell layer during development (Palay & Chan-Palay, 2012). A recent study (Dey et al., 2022) showed that they are in fact relatively common and that they behave electrophysiologically like typical granule cells located in the granule cell layer. The MCG/MLI ratio of our dataset was 32%, which is similar to a previous quantification for the posterior lobe of the cerebellum from which our sample was derived (Dey et al., 2022). As mentioned, these neurons lack PV labeling in their cell bodies (Figure 5 f; Sup. Figure 16 f, g). Their cell bodies share ultrastructural features with typical granule cells. For example, they had round nuclear membranes without infoldings and only a small rim of cytoplasm surrounding the nucleus (Figure 5 g; Sup. Figure 16 h, i). Reconstruction of three MGCs showed that their 3D morphology was also similar to that of granule cells (Figure 5 h). They possessed several short dendrites, each forming a loosely organized glomerulus (Sup. Figure 16 j, insets 1, 2). At least sometimes the glomeruli were associated with mossy fiber collaterals that reached the Purkinje cell layer or slightly above (Sup. Figure 16 j, insets 3, 4). This is expected based on previous descriptions of mossy fibers (Palay & Chan-Palay, 2012). Interestingly, the MGC dendrites were also innervated by parallel fibers. This has not been reported previously and is never the case for typical granule cells (Figure 5 h to j).

Kv1.2: This protein is a member of the voltage-gated potassium channel subfamily A (Trimmer, 2015), and shows high expression in the axonal terminals of the MLIs that form pinceau structures around Purkinje cell axon initial segments (AIS), as indicated by the strong yellow fluorescence signal in Figure 6 a and the reconstruction shown in Figure 6 b, c (Bobik et al., 2004; Laube et al., 1996). These axons are of different caliber (Sup. Figure 17 a-1 to a-7), and none are downstream branches of the same axon,

which may mean that they each come from a different MLI cell. Kv1.2 also has been reported to be present in small puncta in the granule layer at juxtaparanodes of axons of unknown identity (McNamara et al., 1996). We examined 22 sites of juxtaparanodal puncta in 22 axons in the granule layer. Consistent with previous reports (McNamara et al., 1996; Trimmer, 2015), we found 15 pairs of puncta that corresponded to the juxtaparanodal portion of nodes of Ranvier (Figure 6 d to j). In addition, we found 2 sites with three puncta that corresponded to the juxtaparanodal portion of nodes of Ranvier that are at branch points (Sup. Figure 17 b); Finally, we found 5 sites with a single punctum, which corresponded to the final myelinated site of an axon where myelination ended, a hemi-node of Ranvier (Sup. Figure 17 c). From the ssEM, we reconstructed these labeled axons. Six out of 22 had *en passant* or terminal axonal arborizations in the granule cell layer (Figure 6 k; Sup. Figure 17c), suggesting that they are mossy fibers. The remainder of the axons which had a similar appearance ultrastructurally but ran out of our EM volume prevented an unambiguous identification of their type, but they could also be mossy fibers. None of these axons were calbindin-positive. Axons that we suspect are primary Purkinje cell axons or their branches (because they were calbindin positive; Sup. Figure 14 a, inset 2) did not show Kv1.2 labeling at their juxtaparanodes. We thus conclude that at least a portion of the axons with Kv1.2 positive juxtaparanodes are mossy fibers, but not Purkinje cell axons.

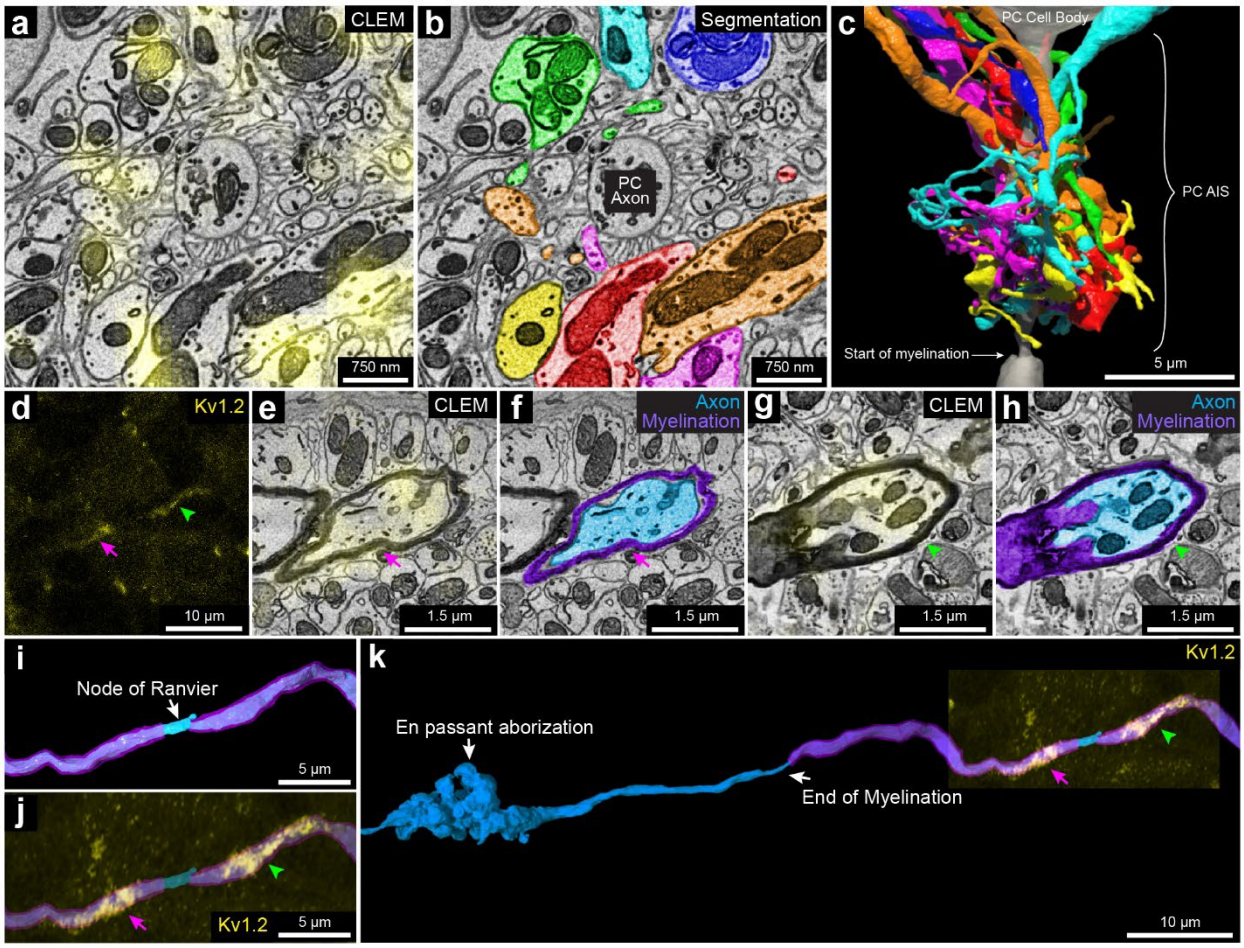

Figure 6. 3D reconstruction of subcellular components with the Kv1.2-specific scFv probe in cerebellum.

a, 2D CLEM image showing the fluorescence signals (yellow) of the Kv1.2-specific scFv probe overlaps with axonal terminals of MLIs at a pinceau structure surrounding the axon initial segment of a Purkinje cell. **b**, EM image showing the 2D segmentations of some (n=7) of the axon terminals labeled in **a**. **c**, 3D reconstruction of the seven axonal terminals in **b** (see Sup. Figure 17 a for the morphology of these axonal terminals). **d**, A pair of juxtaparanodal punctate labeling sites of the Kv1.2-specific scFv probe in the granule cell layer within the confocal image stack. The magenta arrow and green arrowhead show each side of the juxtaparanodal labeling. **e**, 2D CLEM image showing one side of the juxtaparanodal punctate labeling (yellow, magenta arrow) of the axon in **d**. **f**, Shows the 2D segmentation of the axon in **e**. **g**, 2D CLEM image showing another side of the juxtaparanodal punctate labeling (yellow, green arrowhead) of the Kv 1.2-specific scFv probe at the other side of the juxtaparanodal segment of the same node of Ranvier. **h**, EM image showing the 2D segmentation of the axon in **g**. **i**, 3D reconstruction of the node of Ranvier of the axon labeled in **d-h** (myelination labeled in purple). **j,** The juxtaparanodal labeling by the Kv1.2-specific probe in **d** overlaid onto the reconstructed node of Ranvier. **k**, More extended 3D reconstruction of the axon in **i** shows that it had an en passant arborization and another terminal arborization (not shown) in the granule cell layer, that appeared to be mossy fiber synapses.

VGluT1: VGluT1 is a member of the vesicular glutamate transporter family that is expressed by axonal terminals (Fremeau et al., 2004). In the cerebellar cortex, VgluT1 is highly expressed in the boutons of parallel fibers and in a subgroup of mossy fiber arborizations (Fremeau et al., 2004; Gebre et al., 2012). In Crus 1, both in a previous study (Gebre et al., 2012) and in our immunofluorescence images, there are at least three types of mossy fiber arborizations in the granule cell layer: VGluT1 positive, VGluT2 positive, VGluT1/2 double positive terminals (Figure 7 a, c; Sup. Figure 18 a, b-1 to b-3). In our vCLEM dataset, the labeling of anti-VGluT1 scFv in the granule cell layer (cyan fluorescence signal in Figure 7 a) does not label all mossy fibers (Figure 7 c). We classified the mossy fiber arborizations based on whether they were VGluT1 positive (Figure 7 a, b) or VGluT1 negative (Figure 7 c, d). While we can't further subdivide the VGluT1 positive from the VGluT1/2 double positive types, we surmise that the VGluT1 negative terminals are VGluT 2 positive. To see if these two categories had ultrastructural differences, we randomly chose ten VGluT1 positive and ten VGluT1 negative mossy fiber terminals and reconstructed them. The 3D morphologies of both types were similar (Figure 7 e to g). However, the mean volumes of VGluT1 positive terminals were significantly larger than VGluT1 negative terminals ($p < 0.05$) (Figure 7 h) (see Sup. Table 4 and 5 for the volumes of each terminal). We also performed automatic detection of synaptic vesicle (Sup. Figure 18 c, e) and mitochondria in these terminals (Sup. Figure 18 d, f) using machine learning algorithms (see Sup. Table 4 and 5 for the vesicle number, vesicle density, mitochondria volume, and the mitochondria per terminal volume of each terminal). The mean value of the number of synaptic vesicles per terminal was significantly higher in VGluT1 positive terminals than in VGluT1 negative terminals ($p < 0.01$) (Figure 7 i). The mean value of the synaptic density per terminal trended higher in VGluT1 positive terminals than in VGluT1 negative terminals ($p < 0.1$) (Figure 7 j). The mean value of the mitochondria per terminal volume was not significantly different ($p > 0.1$) (Figure 7 k). These results suggest that these two types of mossy fiber terminals have distinct EM ultrastructure. They may originate from different brain regions, have different electrophysiology properties, and/or prefer to synapse with different subgroups of granule cells.

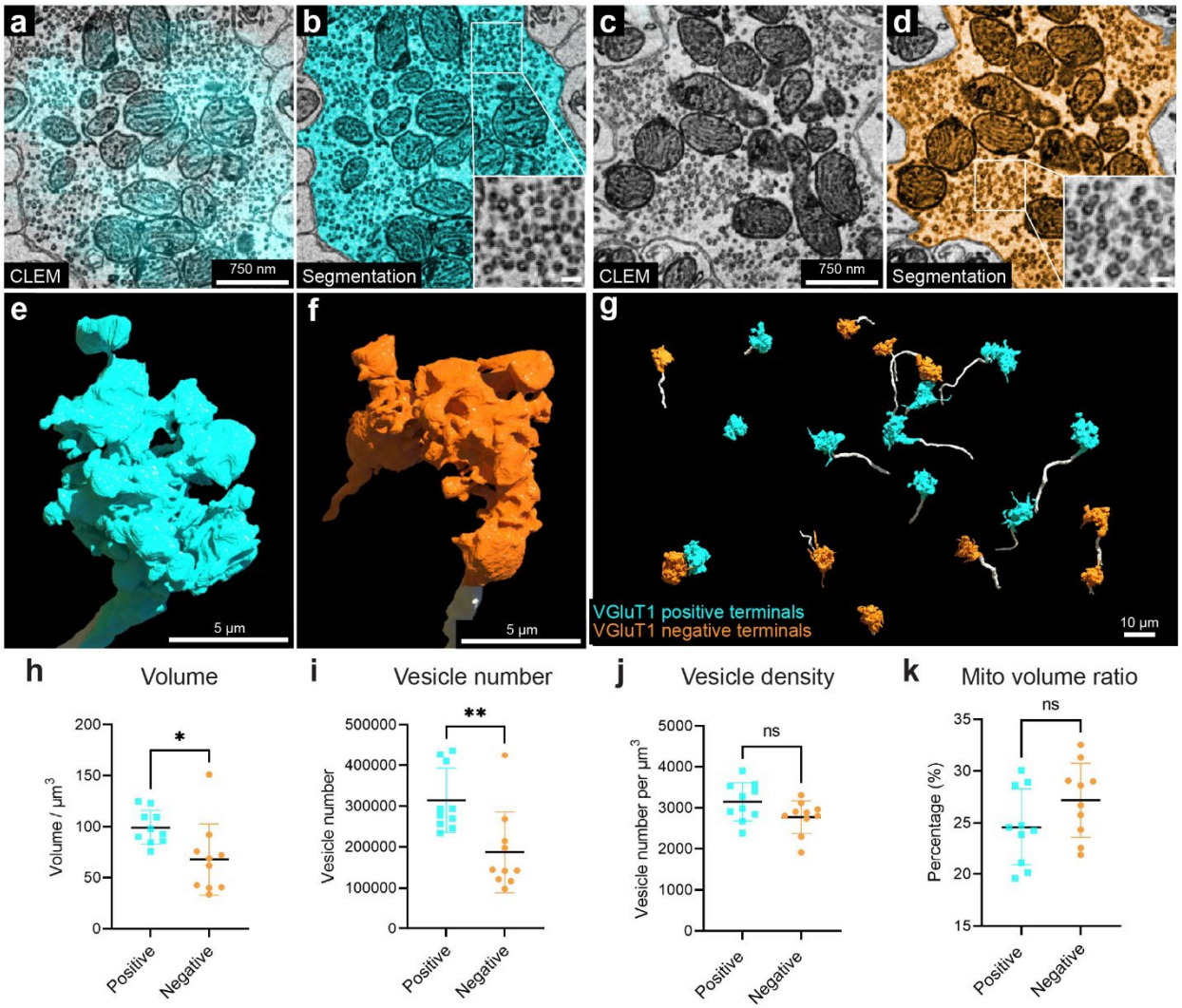

Figure 7. 3D reconstruction and analysis of VGluT1 positive and negative mossy fiber terminals based on labeling with the VGluT1-specific scFv probe.

a, 2D CLEM image showing the fluorescence signals (cyan) of the VGluT1-specific scFv probe overlaps with a mossy fiber terminal. **b**, EM image showing the 2D segmentation (cyan) of the mossy fiber terminal labeled in **a**. The enlarged inset shows the morphology of synaptic vesicles in this terminal. **c**, 2D CLEM image showing a mossy fiber terminal lacking VGluT1 fluorescence signal. **d**, EM image showing the 2D segmentation (orange) of the mossy fiber terminal labeled in **c**. The enlarged inset shows the morphology of synaptic vesicles in this terminal. **e**, 3D reconstruction of the VGLUT1 positive mossy fiber terminal (cyan) in **b**. The axon leading to the terminal arises from the bottom of the panel. **f**, 3D reconstruction of the VGluT1 negative mossy fiber terminal (orange) in **c**. The axon leading to the terminal arises from the bottom of the panel. **g**, 3D reconstruction of ten VGluT1 positive mossy fiber terminals (cyan) and ten VGluT1 negative mossy fiber terminals (orange). The axons are labeled in white. **h**, volume, **i**, vesicle number, **j**, versicle density, **k**, mitochondria volume ratio per terminal volume were measured for each of the 10 VGluT1 positive terminals, cyan, and the 10 VGluT1 negative terminals, orange. Mito, mitochondria.

Discussion

Here we report a technique that visualizes multiple molecular labels superimposed on an electron microscopic volume, using detergent-free scFv-based immunofluorescence. We used this method to study a volume of cerebellum labeled with five scFv probes, acquired by serial section electron microscopy. This vCLEM dataset provided several new insights relevant for the cytology of cerebellar cortex. We will deposit the expression plasmids of eight scFv probes in an open access repository (*Addgene*, n.d.). All of these probes possess a sortase tag to allow straightforward installation of fluorescent or other labels for use in vCLEM studies or other applications.

Expanding this technique will require acquiring a larger collection of functional scFv probes to include more commonly used molecular markers in bioscience. The scFv probes we generated were all based on mAbs from NeuroMab (*UC Davis/NIH NeuroMab Facility*, n.d.). This facility has developed thousands of mAbs for neuroscience research, a subset of which have been converted into recombinant form (Andrews et al., 2019). Consistent with the overall track record of converting mAbs into scFvs (Kontermann & Dübel, 2013), our current efforts to systematically convert NeuroMab mAbs into scFvs that retain the binding characteristics of the progenitor mAb is ~ 50% (J. S. T.; unpublished data). All of the scFvs described here label brain tissue. To generate yet more scFvs, several strategies present themselves. First, *de novo* amino acid sequencing of a mAb can establish the sequences of the V_H and V_L domains of other commonly used mAbs or even individual components of polyclonal Abs for subsequent conversion into scFvs (McDonald et al., n.d.; Perez-Witzke et al., n.d.). Second, artificial protein evolution using phage-display methods has been used to modify the structure of failed scFvs to render them functional (Morrison et al., 2021). Third, rational protein design via point-mutation or CDR-grafting has been used to improve the performance of failed scFvs (Baran et al., 2017; Honegger, 2008). Finally, purely *in vitro* approaches using phage display or other methods can be used to screen naïve or immune scFv libraries to develop novel scFvs (Nissim et al., 1994). We therefore anticipate that more functional scFv probes will become available, in particular through open access sources.

Multiplexability, i.e., multiple labels with different colors, can make vCLEM more cost-effective and more powerful. More resolvable color labels in a specimen means that more molecular information can be extracted without the need of multiple samples. Moreover, combinatorial labels may parse more

cell types than possible with only a single label at a time. For example, in the cerebellum, cells that are calbindin- and PV-positive are Purkinje cells, whereas PV-positive, but calbindin-negative cells, are molecular layer interneurons. This same combinatorial approach will likely be useful in parsing various subtypes of interneurons in the cerebral cortex.

With spectral imaging and linear unmixing, we were able to acquire six-color fluorescent image volumes from samples immunolabeled with scFv probes. However, six-color images are not the upper limit of how many colors can be disambiguated. With the growing list of functional scFvs, optimized algorithms of linear unmixing can achieve super-multiplexed fluorescence imaging with up to 45 colors (Seo et al., 2022). It is possible that scFvs could also be conjugated with narrow-peaked Raman imaging dyes to achieve multiplexed Raman vibrational imaging with 24 or more colors (L. Wei et al., 2017). In addition, as our technique is based on immunolabeling, it can be easily combined with other types of functional vCLEM. For example, scFv-enabled immunofluorescence can be applied to samples that have been functionally imaged with calcium or voltage indicators (Fan et al., 2020), so that the molecular identities of the neurons whose functional properties have been analyzed can also be determined. This advantage can greatly expand the knowledge of neural networks examined by functional live imaging.

We used confocal microscopy to acquire fluorescence volumes of scFv-labeled samples because of the power of linear unmixing to separate multicolor fluorescence. The superior penetration ability of scFvs as demonstrated in this study already exceeds the imaging depth of confocal microscopy of uncleared tissue. Our approach generates usable vCLEM volumes up to a depth of 120 μm. Even deeper imaging may be possible with spectral unmixing techniques for two-photon and light sheet microscopies (Jahr et al., 2015; Rakhymzhan et al., 2021).

With the rapid progress in ssEM, very large datasets (~1 mm^3) (MICrONS Consortium et al., 2021; Shapson-Coe et al., 2021) are being generated. However, the generation of vCLEM datasets of such sizes is technically problematic. The use of scFv labels, once associated with electron microscopy ultrastructure, may circumvent this problem. For example, the cerebellar cortex dataset showed that despite their similar location, the cell bodies of Bergmann glia, MLIs and MGCs were distinct (Figure 4 l; Figure 5 a, b, f, g) and could conceivably be used to train a classifier for determination of cell type. Indeed, using machine learning we could differentiate two molecularly defined mossy terminal types,

despite them having the same neurotransmitter and being functionally and gross-anatomically similar (Figure 7). More recent machine learning algorithms like “SegCLR” (Dorkenwald et al., 2022) use data from small volumes and then identified cell types in large volumes. We believe that the growing number of probes for vCLEM, combined with machine learning, will allow the classification of cellular and subcellular molecular types in unlabeled electron microscopy images.

Methods

Animals

Animals used in the study were adult C58BL/6J mice (Jackson Laboratory). All experiments using animals were conducted according to US National Institutes of Health guidelines and approved by the Committee on Animal Care at Harvard University.

ScFv production

The amino acid sequence of scFv was designed by linking the variable domains of the heavy chain and the light chain of a mAb with a (GGGGS) x 3 or a (GGGGS) x 4 linker. A signal peptide (MDWTWRILFLVAAATGAHS or MGWSCIILFLVATATGVHS) was added to the N’-terminus. A sortase tag (SLPETGG) and a 6 x His tag was added to the C’-terminus. The amino acid sequence was reverse translated into a DNA sequence with codon optimization for human cells. The DNA sequence was synthesized and cloned into pcDNA 3.1 or pcDNA 3.4 vectors.

Expi 293 cells (ThermoFisher) were used for scFv expression. The cells were maintained in Expi 293 Expression Medium (ThermoFisher) and passaged every other day. After two rounds of passage, transfection of the scFv expression plasmids was carried out using 293fectin (ThermoFisher) following vendor’s protocol. For 100 ml culture with 1x 10^8 cells, we used 100 µg plasmid DNA and 200 µl 293fectin. Cells were incubated for another seven days, after which the culture supernatant was collected. The supernatant was incubated with Ni-NTA agarose (ThermoFisher). After washing with Tris buffer (50 mM Tris, 150 mM NaCl, pH = 7.5~8.0), the bound proteins were eluted with the elution buffer (250 mM imidazole, 50 mM Tris, 150 mM NaCl, pH = 7.5~8.0). The eluted proteins were loaded into Amicon® Ultra-15 centrifugal filter unit (Millipore Sigma), washed with Tris buffer, and then buffer

exchanged into Tris buffer with 15% glycerol by centrifugation at 4000 rpm at 4 °C. The concentration of the purified protein was determined by A280. The purified protein was stored at -20 °C.

Sortase reaction

The GGGC peptide was synthesized at BIOMATIK. The GGGC peptides were dissolved in 1 x PBS (Sigma-Aldrich) at the concentration of 20 mg/ml. The fluorescent dyes in maleimide form (ThermoFisher) were dissolved in DMSO at the concentration of 20 mM. The dissolved peptide and fluorescent dyes were mixed at the molar ratio of 12:1 and then incubated with shaking at 800 rpm at 4 °C overnight. The GGGC-dye conjugates were purified by HPLC at the Koch Institute at MIT. Identity of the purified conjugates were confirmed by mass spectroscopy, lyophilized, and then re-dissolved in ddH_2O at the concentration of 4 mM.

The sortase reaction was performed as described in (Antos et al., 2017). In brief, GGGC-dye conjugates (500 uM) and sortase tag-containing scFvs (100 uM) were mixed in the sortase reaction buffer (50 mM Tris-HCl, 150 mM NaCl, 10 mM $CaCl_2$, pH = 7.5~8.0), followed by adding sortase A pentamutant that has a 6 x His tag (2.5 uM). The mixture was incubated with shaking at 500 rpm at 12 °C for 3 h. Then Ni-NTA agarose was added into the mixture, followed by an incubation shaking at 500 rpm at RT for 20 min to remove sortase and any leftover GGGC-dye conjugates. After the incubation, the mixture was loaded into a microcentrifuge spin column (USA Scientific) and centrifuged briefly to remove the Ni-NTA agarose. The filtered solution that contains the scFv-dye conjugates was loaded into Amicon® Ultra-4 centrifugal filter unit (Millipore Sigma), washed with Tris buffer and then buffer exchanged into Tris buffer with 15% glycerol by centrifugation at 4000 rpm at 4 °C. The concentration of the purified scFv-dye conjugates was determined by A280. The purified scFv-dye conjugates were stored at -20 °C.

Perfusion and fixation

The mouse was anesthetized by isoflurane until there was no toe-pinch reflex. Mice were then transcardially perfused with aCSF (125 mM NaCl, 26 mM $NaHCO_3$, 1.25 mM NaH_2PO_4, 2.5 mM KCl, 26 mM glucose, 1 mM $MgCl_2$ and 2 mM $CaCl_2$ (all chemicals were from Sigma-Aldrich) at the flow rate of 10 ml/min for 2 min to remove blood, followed with 4% paraformaldehyde (Electron Microscopy Sciences), 0.1% glutaraldehyde (Electron Microscopy Sciences) in 1 x PBS for 3 min for fixation. Brains were dissected and then post-fixed in the same fixative on a rotator overnight at 4°C. Brains were sectioned

into 50-μm or 120-μm coronal sections using a Leica VT1000 S vibratome and stored in the same fixative at 4°C.

For ECS-preserving perfusion, the detailed protocol was described in (Lu et al., 2023). In brief, mice were anesthetized by isoflurane, transcardially perfused with aCSF at the flow rate of 10 ml/min for 2 min to remove blood, followed with 15 w/v% mannitol (Sigma-Aldrich) aCSF solution for 1 min, 4 w/v% mannitol aCSF solution for 5 min, and 4 w/v% mannitol, 4% paraformaldehyde in 1 x PBS for 5 min. Brains were dissected out and then post-fixed in the same fixative for 3 h on a rotator at 4 °C. Brains were sectioned into 50-μm coronal sections using a Leica VT1000 S vibratome, and then store in in 1 x PBS at 4 °C.

Immunofluorescence

Detergent-free immunofluorescence labeling was performed with scFv probes or nanobody probes (see Sup. Table 1 for the scFv and nanobody probes used in this study). The detailed protocol was described in (Fang et al., 2018). In brief, 50-μm or 120-μm coronal sections were transferred into 3.7 ml shell vials (Electron Microscopy Sciences) with 1 ml 1 x PBS. The sections were first washed with 1 x PBS for 3 x 10 min, and then blocked in glycine blocking buffer (0.1 M glycine, 0.05% NaN_3 in 1 x PBS) for 1 h on a rotator at 4 °C. The labeling solution was prepared by diluting scFv-dye conjugates or nanobody-dye conjugates in glycine blocking buffer (see Sup. Table 1 for the final concentration of each scFv and nanobody probe). The labeling solution and any remaining steps were protected from light. The sections were then incubated with the labeling solution on a rotator at 4 °C. 50-μm sections were incubated for 3 days. 120-μm sections were incubated for 7 days. After the incubation, sections were washed with 1 x PBS for 3 x 10 min, and then stained with Hoechst 33342 (Invitrogen, diluted 1:5000 in 1 x PBS) for 1 h on a rotator at 4 °C. Sections were washed with 1 x PBS for 3 x 10 min, and then mounted onto glass slides (VWR).

Immunofluorescence labeling with detergent was performed with primary antibodies plus secondary antibodies for single labeling (for the validation of scFv probes versus mAbs; see Sup. Figure 2-4), or with primary antibodies plus secondary antibodies and scFv probes for double labeling (for the double labeling experiment of VGluT1 and VGuT2; see Sup. Figure 18) (see Sup. Table 2 for the primary antibodies and Sup. Table 3 for the secondary antibodies used in this study). The detailed protocol is

available on the NeuroMab website (*Immunofluorescence Labeling of Free-Floating Perfusion-Fixed Brain Sections*, 2016). In brief, 50-μm coronal sections were transferred into 3.7 ml shell vials with 1 ml 1 x PBS. The sections were first washed with 1 x PBS for 3 x 10 min, and then blocked in vehicle (10% normal goat serum, 0.3% Triton X-100 in 1 x PBS) overnight on a rotator at 4 °C. Subsequent steps were protected from light. The sections were then incubated with the primary antibody solution or primary antibody solution plus scFv probes (for the experiment of the double labeling of VGluT1 and VGuT2; see Sup. Figure 18) (see Sup. Table 1, 2 for the dilution ratios of primary antibodies and the anti-VGluT 1 scFv probe used in this study;) for 2 days on a rotator at 4 °C. After the incubation, sections were washed with vehicle for 3 x 10 min, and then incubated with the secondary antibody solution (see Sup. Table 3 for the dilution ratios of secondary antibodies used in this study) overnight on a rotator at 4 °C. After the incubation, sections were washed with 1 x PBS for 3 x 10 min, and then stained with Hoechst (diluted 1:5000 in 1 x PBS) for 1 h on a rotator at 4 °C. Sections were washed with 1 x PBS for 3 x 10 min, and then mounted onto glass slides.

Fluorescence confocal microscopy

50-μm sections were mounted in Vectashield H-1000 (Vector Laboratories) with a #1 coverslip (Electron Microscopy Sciences) on top sealed with clear nail polish. 120-μm sections (for CLEM) were mounted in 1 x PBS inside 120-um spacer (Invitrogen) with a #1 coverslip on top sealed with the spacer. 50-μm sections were imaged with a Zeiss LSM 880 confocal laser scanning microscope equipped with either a 20x/0.8 NA air-objective, or a 40x/1.1 NA water immersion objective, or a 63x/1.4 NA oil-immersion objective depending on the required optical resolution. Acquisition of double or triple color fluorescent images was done with appropriate band pass filters for the specific fluorescent dyes to avoid crosstalk.

For spectral imaging, the detailed protocol was described in (Lelouard et al., n.d.).In brief, 120-μm sections immunolabeled by five scFv with different fluorescent dyes (Alexa fluor 488, 532, 594, 647, and 5-TAMRA) were imaged with a Zeiss LSM 880 confocal laser scanning microscope equipped with a 40x/1.1 NA water immersion objective. All fluorophores except Hoechst were excited simultaneously with 488, 560, 633 nm lasers and a 488/561/633 nm beam splitter. A z-stack of lambda stack images with the interval of 1 μm in z axis was acquired by an array of 32 Gallium Arsenide Phosphide (GaAsP) detectors

in lambda mode at 9nm bins from 414 nm to 691 nm. Lambda stack images were acquired from each of the sections labeled by only one of the five scFvs with the same settings in lambda mode. Reference spectra for each fluorescent dye were extracted from each of these lambda stacks. Linear unmixing was performed on the z-stack of lambda stack images acquired from the multi-labelled section using the reference spectra in Zen Blue software (Zeiss). The Hoechst channel (labeling cell nuclei) of the multi-labelled section was acquired separately with a single 405 nm laser and appropriate band pass filters.

To test if the Hoechst channel could be combined into linear unmixing, we tried acquiring another z-stack of lambda stack images of another multi-labeled 120-μm section with simultaneous excitation with 405, 488, 560, 633 nm lasers, a 488/561/633 nm beam splitter and a 405 nm beam splitter. A lambda stack image was acquired from a section labeled by only Hoechst with the same settings in lambda mode. Linear unmixing was performed on the z-stack of lambda stack images of the multi-labelled section using the reference spectra (five fluorescent dyes plus Hoechst) in Zen Blue software (Zeiss). Several reference spectra for Hoechst extracted from different locations of pixels in Hoechst's lambda stack image caused the Hoechst signals to be unmixed into the channel of Alexa 488 in error, but we did find one spectrum that generated good unmixing results (Sup. Figure 5).

The brightness, contrast, and gamma of all fluorescent images were adjusted. Fluorescence image volumes were projected to a single plane by maximum intensity for visualization in 2D.

ScFv, nanobody, and antibody penetration experiment

Immunofluorescence with or without detergent by scFv probes, nanobody probes, primary antibodies with dyes directly conjugated, or with primary antibodies plus secondary antibodies was performed on 300-μm coronal sections from animals perfused with normal or ECS-preserving protocol. See above for detailed protocol of immunofluorescence. For the sections labeled with scFv probes, nanobody probes, primary antibodies with dyes directly conjugated, the incubation lasted for 7 days. For the sections labeled with the primary mAb for calbindin, the sections were incubated with the primary antibody solution (see Sup. Table 2 for the dilution ratio of this mAb) for 4 days on a rotator at 4 °C. After the incubation, sections were washed with vehicle for 3 x 10 min, and then incubated with the secondary antibody solution (see Sup. Table 3 for the dilution ratio of the secondary antibody) for 3 days on a rotator at 4 °C. After the incubation, sections were washed with 1 x PBS for 3 x 10 min. Then the sections were

sliced into 50-μm sections lengthwise using a VT1000 S vibratome. The section from the middle was mounted onto glass slides, and then imaged by confocal microscopy to evaluate the penetration depth.

EM preparation

After 120-μm sections were imaged, a small amount of 1 x PBS was added between the glass and coverslip to unseal the coverslip. Sections were transferred into 3.7 ml shell vials with 1 ml secondary fixative (2% PFA, 2,5% glutaraldehyde in 0.15M sodium cacodylate buffer with 4mM Ca^{2+} and 0.4 mM Mg^{2+}) and incubated for at least one week on a rotator at 4 °C. A modified ROTO (Reduced Osmium-Thiocarbohydrazide-Osmium) protocol was used to stain the sections. All steps were carried out at room temperature (RT) except when specified. Sections were washed 3 x 10 min in 0.15 M sodium cacodylate buffer with 4 mM Ca^{2+} and 0.4 mM Mg^{2+}, and then incubated in a solution containing 2 w/v% OsO_4 (Electron Microscopy Sciences), 1.5% w/v potassium ferrocyanide (Sigma-Aldrich) and 0.15M cacodylate buffer inside 120-μm spacers (the top surfaces were not peeled) between a glass slide and a coverslip for 2 h with a change of the same solution after the first hour to prevents tissue deformation. Sections were incubated in the same solution in shell vials for another 1.5 h on a rotator. After washing 3 x 10 min in ddH_2O, sections were incubated in a filtered aqueous solution containing 1 w/v% thiocarbohydrazide (Sigma-Aldrich) for 45 min. After washing 3 x 10 min in ddH_2O, sections were incubated in an aqueous solution containing 2 w/v% OsO_4 for 1.5 h. After washing 3 x 10 min in ddH_2O, sections were incubated in a filtered aqueous solution containing 1 w/v% uranyl acetate (Electron Microscopy Sciences) overnight on a rotator protected from light. On the next day, after washing 3 x 10 min in ddH_2O, sections were dehydrated in a series of graded (25, 50, 75, 100, 100, 100 v/v%, 10 min each) acetonitrile (Electron Microscopy Sciences) aqueous solutions. Afterward, sections were infiltrated with 25% LX-112 (Ladd Research) : acetonitrile for 1.5 h, 50% LX-112 : acetonitrile for 3 h, 75% LX-112 : acetonitrile overnight, 100% LX-112 for 12 h on a rotator. Then the sections were embedded in 100% LX-112 at the bottom of a flat bottom embedding capsule (Electron Microscopy Sciences) and cured in a 60 °C oven for two days.

X-ray MicroCT scanning

X-ray micro-computed tomography (μCT) images of the resin-embedded sections were acquired using a Zeiss Xradia 510 Versa system and Zeiss' Scout and Scan software. The imaging conditions include a projection pixel size of around 1.15 μm (pixel bin size of 1), 60 kV x-ray source, 30 s exposure

per projection, and 3501 projections for 360 degrees of rotation. Each scan took approximately 33 hours. The Feldkamp, Davis, and Kress (FDK) algorithm reconstructed 3-dimensional volume maintains the projection pixel size of 1.15 μm resulting in a voxel size of 1.15 μm^3. The Scout and Scan Control System Reconstructor software was used to convert the reconstructed files to .tiff files.

EM imaging

The resin-embedded sections were cut into 30 nm serial ultrathin sections using automated tape-collecting ultramicrotome (ATUM) (Kasthuri et al., 2015). Serial sections were collected onto carbon-coated and plasma-treated Kapton tape. The tape was cut into strips and affixed onto 150 mm silicon wafers (University Wafer).

A Zeiss Sigma scanning electron microscope was used to acquire overview images from the serial sections. Two overview images were taken per wafer, which were around 1.35 μm apart in z-axis. Typical imaging conditions are 8-kV landing energy, 1.2-nA beam current, 3-μs dwell time, 150-nm pixel size, and 4k x 4k images. The images were captured using a below-the-lens backscatter detector and Zeiss' Atlas 5 software. The overview images were aligned using the "Linear stack alignment with SIFT" plugin in FIJI.

Prior to acquiring high-resolution images, the serial section sections on wafers were post-stained for 4 min with a 3% lead citrate solution. After staining, the sections were degassed for a minimum of 24 h at 1x10-6 Torr. A Zeiss MultiSEM 505 scanning electron microscope equipped with 61 electron beams was used to acquire high-resolution images from the serial sections. Images were collected using a 1.5-kV landing energy, 4-nm image pixel, and a 400-ns dwell time.

High-resolution EM image processing

The preparation of the ssEM data before it could be segmented/analyzed includes two steps: affine stitching and elastic alignment. Affine stitching was performed on the raw data coming from the microscope. Firstly, SIFT features were extracted from the boundary area of each raw tile. Then all the neighborhood tiles in each section were matched together based on SIFT feature matching. Finally, a global optimization step made the matching results smooth. After each section was stitched well, an elastic alignment of all the sections was performed. A rough affine transformation between each mFov in section i to section i+1 and i+2 was estimated based on the SIFT features of blob-like objects detected in

the sections. Then template matching, performed as a fine-grained matching for section i to section i+1 and i+2, was done on grid distributed image blocks in section i. At last, a global optimization on all the sections in the whole stack made the elastic transformation of mesh grid points on all the sections smooth.

The aligned stack was rendered at full resolution (4 x 4 x 30 nm) and each section was cut into 4k x 4k .png tiles, imported into VAST as a .vsvi file, and ingested into Neuroglancer for further analysis.

Co-registration of fluorescence and EM volumes

The ssEM volume at a downsampled pixel size of 128 nm in the x and y plane and 480 nm in the z-axis was exported from the high-resolution .vsv file in VAST. The multi-color fluorescent image volume's brightness and contrast were adjusted with the "Stack contrast adjustment" plugin in FIJI to compensate for signal decay in the z-axis. The pixel sizes in the x and y plane and in the z-axis were resampled to match those of the confocal fluorescence image volume. Both volumes were loaded into FIJI. With the BigWarp plugin, 188 landmark points were manually placed on corresponding sites of blood vessels, cell nuclei, cell bodies, and axons in the two volumes. The fluorescent image volume was 3D transformed by a thin plate spline interpolation based on the point correspondences. The transformed fluorescence volume was resampled in the z-axis and then imported into VAST as .vsv files to be overlaid with the ssEM volume at a downsampled pixel size of 128 nm in the x and y plane and 30 nm in the z-axis. The .vsv files were also ingested into Neuroglancer and resampled in the z-axis to be overlaid with the ssEM volume at a pixel size of 8 nm in the x and y plane and 30 nm in the z-axis.

Automatic segmentation

The ssEM dataset was segmented in 3D using Flood-Filling Networks (FFNs) (Januszewski et al., 2018). The FFN segmentation model was trained at 32 x 32 x 30 or 16 x 16 x 30 nm resolution on the H01 dataset (Shapson-Coe et al., 2021), and run here on CLAHE intensity normalized data (Zuiderveld, 1994) downsampled to match the trained model resolution. The resulting base supervoxels were assembled into larger per-cell segments via manual proofreading.

The ssEM dataset was also segmented in 2D at 8 x 8 x 30 nm resolution by a method developed in our lab. A description of this approach was given in (Karlupia et al., 2023; Meirovitch et al., 2018). In brief, a pre-trained algorithm was used to generate ground truth tiles of membrane predictions, which was

corrected by a human annotator. Three rounds of ground truth correction were used to iteratively train deep neural network (Pavarino et al., 2023) with a UNET architecture (Çiçek et al., 2016). Neural network predictions were done on a commodity GPU using MATLAB connected to a VAST (Berger et al., 2018) instance, serving the EM images. In each round the model was applied on tiles randomly selected from the entire EM space and corrections were made to tiles that contained errors. Producing further training rounds halted when a sufficient accuracy was met. Finally, 2D segmentation using a region-growing algorithm was applied on the entire space according to the local minima of the membrane predictions.

Mitochondria detection

We implemented an anisotropic U-Net architecture, incorporating a combination of 2D and 3D convolutions, to predict binary mitochondrial masks and instance maps similar to the U3D-BC approach in MitoEM (D. Wei et al., 2020). Given that the annotations for the new training dataset are confined to a select number of neurons rather than densely annotated, our model exclusively considers regions containing labeled neurons for loss computation. This strategy prevents the generation of empty predictions for valid mitochondria solely due to the absence of annotations within labeled neurons. To separate individual mitochondria, including those in close proximity, we employ marker-controlled watershed segmentation based on the network's predictions. The segmentation system is implemented with the open-source PyTorch Connectomics deep learning toolbox (Lin et al., 2021).

Vesicle segmentation and visualization

We first saturated segmented all vesicles on six images from a terminal, totaling around 8,400 instances. Then, we fine-tuned the Cytoplasm 2.0 model from Cellpose (Pachitariu & Stringer, 2022; Stringer et al., 2021) on these annotations. Specifically, as the model was pretrained on images with cells of a bigger size, we scaled up our image and segmentation maps of vesicles by 2x in both XY dimensions. For the 20 volumes of terminals, we obtained roughly 5 million vesicle instances.

Statistical analysis

After the brightness of contrast of the layer of the fluorescent signals of VGluT1 were fixed at a value in Neuroglancer, a human annotator randomly picked 10 locations of VGluT1 positive mossy fiber terminals and 10 locations of VGluT1 negative mossy fiber terminals on slice 512 of the ssEM dataset.

After 3D reconstruction of these terminals, the volume size of each terminal was generated using VAST. Mitochondria and synaptic detections (see above) were performed on segmentation of each terminal. None of these approaches were done blind to whether a terminal is VGluT1 positive or negative. Unpaired t-tests on volume, synaptic vesicle number, synaptic density, and mitochondria volume per terminal were performed in Prism-GraphPad.

Acknowledgement

We thank the Harvard Center for Biological Imaging (RRID:SCR_018673) for infrastructure and support, D. Richardson at Harvard Center for Biological Imaging for advice on linear unmixing, the Biopolymers and Proteomics Core Facility at the Koch Institute at MIT for processing the peptide-fluorescent dye conjugates, the Bauer Core Facility at Harvard for infrastructure and support. This work was supported by NIH grants U19 NS104653, UG3 MH123386, P50 MH094271 (J. W. L.), U24 NS109113 (J. S. T.), and K99 MH128891 (X. L.); NSF grants NSF-CAREER-2239688 (D. W.), NCS-FO-2124179, and NCS-FO-1835231 (H. Pfister.); Office of Naval Research grant N00014-20-1-2828 (J. W. L). X. H. was supported by the Edward R. and Anne G. Lefler predoctoral fellowship from the Lefler Center for Neurodegenerative Disorders at Harvard Medical School and the Simmons Awards from the Harvard Center for Biological Imaging.

Author Contribution

X. H., X. L. (xiaotang_lu@fas.harvard.edu), J. W. L, and J. S. T. conceived this study. J. S. T generated the mAb sequences. X. H. generated the scFv probes. T. F. and H. Ploegh provided materials for scFv probe production. X. H. performed the LM experiments. X. H. and R. S. performed the EM experiments. S. W. performed the imaging processing of the ssEM dataset. P. H. L. and V. J. performed 3D segmentation and curated the vCLEM dataset at Neuroglancer. Y. M. (yaron.mr@gmail.com) performed 2D segmentation. D. B. provided the reconstruction tool VAST and advice on 3D reconstruction and rendering. Y. W. helped with LM and EM co-registration. X. H., X. L., E. S. M., and S. A. performed 3D reconstruction and analysis. D. W., Z. L., J. A., and H. Pfister performed mitochondria and vesicle detection. X. H. and J. W. L wrote the paper with input from J. S. T., H. Ploegh., R. S., V. J., and P. H. L.

Competing interests

The authors declare no competing interests.

References

Addgene. (n.d.). Addgene. https://www.addgene.org/

Ahmad, Z. A., Yeap, S. K., Ali, A. M., Ho, W. Y., Alitheen, N. B. M., & Hamid, M. (2012). scFv antibody: principles and clinical application. *Clinical & Developmental Immunology*, *2012*, 980250.

Andressen, C., Blümcke, I., & Celio, M. R. (1993). Calcium-binding proteins: selective markers of nerve cells. *Cell and Tissue Research*, *271*(2), 181–208.

Andrews, N. P., Boeckman, J. X., Manning, C. F., Nguyen, J. T., Bechtold, H., Dumitras, C., Gong, B., Nguyen, K., van der List, D., Murray, K. D., Engebrecht, J., & Trimmer, J. S. (2019). A toolbox of IgG subclass-switched recombinant monoclonal antibodies for enhanced multiplex immunolabeling of brain. *ELife*, *8*. https://doi.org/10.7554/eLife.43322

Antos, J. M., Ingram, J., Fang, T., Pishesha, N., Truttmann, M. C., & Ploegh, H. L. (2017). Site-Specific Protein Labeling via Sortase-Mediated Transpeptidation. In *Current Protocols in Protein Science* (Vol. 89, Issue 1). https://doi.org/10.1002/cpps.38

Bandeira, N., Pham, V., Pevzner, P., Arnott, D., & Lill, J. R. (2008). Automated de novo protein sequencing of monoclonal antibodies. *Nature Biotechnology*, *26*(12), 1336–1338.

Baran, D., Pszolla, M. G., Lapidoth, G. D., Norn, C., Dym, O., Unger, T., Albeck, S., Tyka, M. D., & Fleishman, S. J. (2017). Principles for computational design of binding antibodies. *Proceedings of the National Academy of Sciences of the United States of America*, *114*(41), 10900–10905.

Baude, A., Nusser, Z., Roberts, J. D. B., Mulvihill, E., Jeffrey McIlhinney, R. A., & Somogyi, P. (1993). The metabotropic glutamate receptor (mGluRlα) is concentrated at perisynaptic membrane of neuronal subpopulations as detected by immunogold reaction. *Neuron*, *11*(4), 771–787.

Begemann, I., & Galic, M. (2016). Correlative Light Electron Microscopy: Connecting Synaptic Structure and Function. *Frontiers in Synaptic Neuroscience*, *8*, 28.

Berciano, M. T., & Lafarga, M. (1988). Colony-forming ectopic granule cells in the cerebellar primary fissure of normal adult rats: a morphologic and morphometric study. *Brain Research*, *439*(1–2), 169–178.

Berger, D. R., Sebastian Seung, H., & Lichtman, J. W. (2018). VAST (Volume Annotation and Segmentation Tool): Efficient Manual and Semi-Automatic Labeling of Large 3D Image Stacks. In *Frontiers in Neural Circuits* (Vol. 12). https://doi.org/10.3389/fncir.2018.00088

Bignami, A., & Dahl, D. (1973). Differentiation of astrocytes in the cerebellar cortex and the pyramidal tracts of the newborn rat. An immunofluorescence study with antibodies to a protein specific to astrocytes. In *Brain Research* (Vol. 49, Issue 2, pp. 393–402). https://doi.org/10.1016/0006-8993(73)90430-7

Bignami, A., Eng, L. F., Dahl, D., & Uyeda, C. T. (1972). Localization of the glial fibrillary acidic protein in astrocytes by immunofluorescence. *Brain Research*, *43*(2), 429–435.

Bishop, D. L., Misgeld, T., Walsh, M. K., Gan, W.-B., & Lichtman, J. W. (2004). Axon branch removal at developing synapses by axosome shedding. *Neuron*, *44*(4), 651–661.

Bobik, M., Ellisman, M. H., Rudy, B., & Martone, M. E. (2004). Potassium channel subunit Kv3.2 and the water channel aquaporin-4 are selectively localized to cerebellar pinceau. In *Brain Research* (Vol. 1026, Issue 2, pp. 168–178). https://doi.org/10.1016/j.brainres.2004.07.088

Bogovic, J. A., Hanslovsky, P., Wong, A., & Saalfeld, S. (2016). Robust registration of calcium images by learned contrast synthesis. *2016 IEEE 13th International Symposium on Biomedical Imaging (ISBI)*, 1123–1126.

Brandenburg, C., Smith, L. A., Kilander, M. B. C., Bridi, M. S., Lin, Y.-C., Huang, S., & Blatt, G. J. (2021). Parvalbumin subtypes of cerebellar Purkinje cells contribute to differential intrinsic firing properties. *Molecular and Cellular Neurosciences*, *115*, 103650.

Cai, D., Cohen, K. B., Luo, T., Lichtman, J. W., & Sanes, J. R. (2013). Improved tools for the Brainbow toolbox. *Nature Methods*, *10*(6), 540–547.

Celio, M. R. (1990). Calbindin D-28k and parvalbumin in the rat nervous system. *Neuroscience*, *35*(2), 375–475.

Chen, F., Tillberg, P. W., & Boyden, E. S. (2015). Optical imaging. Expansion microscopy. *Science*, *347*(6221), 543–548.

Chen, X., Zaro, J. L., & Shen, W.-C. (2013). Fusion protein linkers: property, design and functionality. *Advanced Drug Delivery Reviews*, *65*(10), 1357–1369.

Chen, Y., Kim, S. H., Shang, Y., Guillory, J., Stinson, J., Zhang, Q., Hötzel, I., & Hoi, K. H. (2018). Barcoded sequencing workflow for high throughput digitization of hybridoma antibody variable domain sequences. *Journal of Immunological Methods*, *455*, 88–94.

Çiçek, Ö., Abdulkadir, A., Lienkamp, S. S., Brox, T., & Ronneberger, O. (2016). 3D U-Net: Learning Dense Volumetric Segmentation from Sparse Annotation. *Medical Image Computing and Computer-Assisted Intervention – MICCAI 2016*, 424–432.

Debs, B. E., Utharala, R., Balyasnikova, I. V., Griffiths, A. D., & Merten, C. A. (2012). Functional single-cell hybridoma screening using droplet-based microfluidics. *Proceedings of the National Academy of Sciences*, *109*(29), 11570–11575.

Dey, M. R., Reddy, K., Yoshida, H., Nishiyama, N., Zemelman, B. V., & Nishiyama, H. (2022). Granule Cells Constitute One of the Major Neuronal Subtypes in the Molecular Layer of the Posterior Cerebellum. *ENeuro*, *9*(3). https://doi.org/10.1523/ENEURO.0289-21.2022

Dorkenwald, S., Li, P. H., Januszewski, M., Berger, D. R., Maitin-Shepard, J., Bodor, A. L., Collman, F., Schneider-Mizell, C. M., da Costa, N. M., Lichtman, J. W., & Jain, V. (2022). Multi-layered maps of neuropil with Segmentation-Guided Contrastive Learning. In *bioRxiv*. https://doi.org/10.1101/2022.03.29.486320

Fan, L. Z., Kheifets, S., Böhm, U. L., Wu, H., Piatkevich, K. D., Xie, M. E., Parot, V., Ha, Y., Evans, K. E., Boyden, E. S., Takesian, A. E., & Cohen, A. E. (2020). All-Optical Electrophysiology Reveals the Role of Lateral Inhibition in Sensory Processing in Cortical Layer 1. *Cell*, *180*(3), 521-535.e18.

Fang, T., Lu, X., Berger, D., Gmeiner, C., Cho, J., Schalek, R., Ploegh, H., & Lichtman, J. (2018). Nanobody immunostaining for correlated light and electron microscopy with preservation of ultrastructure. *Nature Methods*, *15*(12), 1029–1032.

Feng, G., Mellor, R. H., Bernstein, M., Keller-Peck, C., Nguyen, Q. T., Wallace, M., Nerbonne, J. M., Lichtman, J. W., & Sanes, J. R. (2000). Imaging neuronal subsets in transgenic mice expressing multiple spectral variants of GFP. *Neuron*, *28*(1), 41–51.

Fremeau, R. T., Jr, Voglmaier, S., Seal, R. P., & Edwards, R. H. (2004). VGLUTs define subsets of excitatory neurons and suggest novel roles for glutamate. *Trends in Neurosciences*, *27*(2), 98–103.

Fulton, K. A., & Briggman, K. L. (2021). Permeabilization-free en bloc immunohistochemistry for correlative microscopy. *ELife*, *10*. https://doi.org/10.7554/eLife.63392

Garcia-Segura, L. M., Baetens, D., Roth, J., Norman, A. W., & Orci, L. (1984). Immunohistochemical mapping of calcium-binding protein immunoreactivity in the rat central nervous system. In *Brain Research* (Vol. 296, Issue 1, pp. 75–86). https://doi.org/10.1016/0006-8993(84)90512-2

Gebre, S. A., Reeber, S. L., & Sillitoe, R. V. (2012). Parasagittal compartmentation of cerebellar mossy fibers as revealed by the patterned expression of vesicular glutamate transporters VGLUT1 and VGLUT2. *Brain Structure & Function*, *217*(2), 165–180.

German, D. C., Ng, M. C., Liang, C. L., McMahon, A., & Iacopino, A. M. (1997). Calbindin-D28k in nerve cell nuclei. *Neuroscience*, *81*(3), 735–743.

Harlow, E. (1988). Monoclonal antibodies. *Antibodies : A Laboratory Manual.*, 139–243.

Honegger, A. (2008). Engineering antibodies for stability and efficient folding. *Handbook of Experimental Pharmacology*, *181*, 47–68.

Hwang, Y.-S., Maclachlan, C., Blanc, J., Dubois, A., Petersen, C. C. H., Knott, G., & Lee, S.-H. (2021). 3D Ultrastructure of Synaptic Inputs to Distinct GABAergic Neurons in the Mouse Primary Visual Cortex. *Cerebral Cortex* , *31*(5), 2610–2624.

Immunofluorescence Labeling of Free-Floating Perfusion-Fixed Brain Sections. (2016). NeuroMab. chrome-extension://efaidnbmnnnibpcajpcglclefindmkaj/https://neuromab.ucdavis.edu/files/NeuroMab%20brain%20IF%20protocol%200320.pdf

Ingram, J. R., Schmidt, F. I., & Ploegh, H. L. (2018). Exploiting Nanobodies' Singular Traits. *Annual Review of Immunology*, *36*, 695–715.

Jahr, W., Schmid, B., Schmied, C., Fahrbach, F. O., & Huisken, J. (2015). Hyperspectral light sheet microscopy. *Nature Communications*, *6*, 7990.

Januszewski, M., Kornfeld, J., Li, P. H., Pope, A., Blakely, T., Lindsey, L., Maitin-Shepard, J., Tyka, M., Denk, W., & Jain, V. (2018). High-precision automated reconstruction of neurons with flood-filling networks. *Nature Methods*, *15*(8), 605–610.

Joesch, M., Mankus, D., Yamagata, M., Shahbazi, A., Schalek, R., Suissa-Peleg, A., Meister, M., Lichtman, J. W., Scheirer, W. J., & Sanes, J. R. (2016). Reconstruction of genetically identified neurons imaged by serial-section electron microscopy. *ELife*, *5*. https://doi.org/10.7554/eLife.15015

Karlupia, N., Schalek, R. L., Wu, Y., Meirovitch, Y., Wei, D., Charney, A. W., Kopell, B. H., & Lichtman, J. W. (2023). Immersion fixation and staining of multi-cubic millimeter volumes for electron microscopy-based connectomics of human brain biopsies. *Biological Psychiatry*. https://doi.org/10.1016/j.biopsych.2023.01.025

Kasthuri, N., Hayworth, K. J., Berger, D. R., Schalek, R. L., Conchello, J. A., Knowles-Barley, S., Lee, D., Vázquez-Reina, A., Kaynig, V., Jones, T. R., Roberts, M., Morgan, J. L., Tapia, J. C., Seung, H. S., Roncal, W. G., Vogelstein, J. T., Burns, R., Sussman, D. L., Priebe, C. E., … Lichtman, J. W. (2015). Saturated Reconstruction of a Volume of Neocortex. *Cell*, *162*(3), 648–661.

Kim, B. J., Lee, S. Y., Kim, H. W., Park, E.-J., Kim, J., Kim, S. J., So, I., & Jeon, J.-H. (2009). Optimized immunohistochemical analysis of cerebellar purkinje cells using a specific biomarker, calbindin d28k. *The Korean Journal of Physiology & Pharmacology: Official Journal of the Korean Physiological Society and the Korean Society of Pharmacology*, *13*(5), 373–378.

Kontermann, R. E., & Dübel, S. (2013). *Antibody Engineering*. Springer Science & Business Media.

Kosaka, T., Kosaka, K., Nakayama, T., Hunziker, W., & Heizmann, C. W. (1993). Axons and axon terminals of cerebellar Purkinje cells and basket cells have higher levels of parvalbumin immunoreactivity than somata and dendrites: quantitative analysis by immunogold labeling. *Experimental Brain Research. Experimentelle Hirnforschung. Experimentation Cerebrale*, *93*(3), 483–491.

Kozareva, V., Martin, C., Osorno, T., Rudolph, S., Guo, C., Vanderburg, C., Nadaf, N., Regev, A., Regehr, W. G., & Macosko, E. (2022). Author Correction: A transcriptomic atlas of mouse cerebellar cortex comprehensively defines cell types. *Nature*, *602*(7896), E21.

Kuan, A. T., Bondanelli, G., Driscoll, L. N., Han, J., Kim, M., Hildebrand, D. G. C., Graham, B. J., Thomas, L. A., Panzeri, S., Harvey, C. D., & Lee, W.-C. A. (2022). Synaptic wiring motifs in posterior parietal cortex support decision-making. In *bioRxiv*. https://doi.org/10.1101/2022.04.13.488176

Lafarga, M., & Berciano, M. T. (1985). A Golgi and morphometric study of the ectopic granule cells in the molecular layer of the rat cerebellum. *Brain Research*, *345*(2), 398–401.

Laube, G., Röper, J., Pitt, J. C., Sewing, S., Kistner, U., Garner, C. C., Pongs, O., & Veh, R. W. (1996). Ultrastructural localization of Shaker-related potassium channel subunits and synapse-associated protein 90 to septate-like junctions in rat cerebellar Pinceaux. *Brain Research. Molecular Brain Research*, *42*(1), 51–61.

Lee, W.-C. A., Bonin, V., Reed, M., Graham, B. J., Hood, G., Glattfelder, K., & Reid, R. C. (2016). Anatomy and function of an excitatory network in the visual cortex. *Nature*, *532*(7599), 370–374.

Lelouard, H., Mailfert, S., & Fallet, M. (n.d.). A ten-color spectral imaging strategy to reveal localization of gut immune cell subsets. *Zeiss Application Note*.

Lin, Z., Wei, D., Lichtman, J., & Pfister, H. (2021). PyTorch Connectomics: A Scalable and Flexible Segmentation Framework for EM Connectomics. In *arXiv [eess.IV]*. arXiv. http://arxiv.org/abs/2112.05754

Livet, J., Weissman, T. A., Kang, H., Draft, R. W., Lu, J., Bennis, R. A., Sanes, J. R., & Lichtman, J. W. (2007). Transgenic strategies for combinatorial expression of fluorescent proteins in the nervous system. *Nature*, *450*(7166), 56–62.

Lu, X., Han, X., Meirovitch, Y., Sjostedt, E., Schalek, R., & Lichtman, J. (2023). *Preserving extracellular*

space for high-quality optical and ultrastructural studies of whole mammalian brains.

Martell, J. D., Deerinck, T. J., Sancak, Y., Poulos, T. L., Mootha, V. K., Sosinsky, G. E., Ellisman, M. H., & Ting, A. Y. (2012). Engineered ascorbate peroxidase as a genetically encoded reporter for electron microscopy. *Nature Biotechnology*, *30*(11), 1143–1148.

McDonald, Z., Liu, Q., Xie, M., Taylor, P., & Ma, B. (n.d.). *Prevalence of Secondary Light Chains*. Rapid Novor. https://www.rapidnovor.com/prevalence-of-secondary-light-chains-de-novo-sequencing/

McNamara, N. M., Averill, S., Wilkin, G. P., Dolly, J. O., & Priestley, J. V. (1996). Ultrastructural localization of a voltage-gated K+ channel alpha subunit (KV 1.2) in the rat cerebellum. *The European Journal of Neuroscience*, *8*(4), 688–699.

Meirovitch, Y., Mi, L., Saribekyan, H., Matveev, A., Rolnick, D., & Shavit, N. (2018). Cross-classification clustering: An efficient multi-object tracking technique for 3-D instance segmentation in connectomics. In *arXiv [cs.CV]* (pp. 8425–8435). arXiv. http://openaccess.thecvf.com/content_CVPR_2019/html/Meirovitch_Cross-Classification_Clustering_An_Efficient_Multi-Object_Tracking_Technique_for_3-D_Instance_CVPR_2019_paper.html

Michalska, J. M., Lyudchik, J., Velicky, P., Korinkova, H., Watson, J. F., Cenameri, A., Sommer, C., Venturino, A., Roessler, K., Czech, T., Siegert, S., Novarino, G., Jonas, P., & Danzl, J. G. (2022). Uncovering brain tissue architecture across scales with super-resolution light microscopy. In *bioRxiv*. https://doi.org/10.1101/2022.08.17.504272

Micheva, K. D., & Smith, S. J. (2007). Array tomography: a new tool for imaging the molecular architecture and ultrastructure of neural circuits. *Neuron*, *55*(1), 25–36.

MICrONS Consortium, Alexander Bae, J., Baptiste, M., Bodor, A. L., Brittain, D., Buchanan, J., Bumbarger, D. J., Castro, M. A., Celii, B., Cobos, E., Collman, F., da Costa, N. M., Dorkenwald, S., Elabbady, L., Fahey, P. G., Fliss, T., Froudakis, E., Gager, J., Gamlin, C., … Yu, S.-C. (2021). Functional connectomics spanning multiple areas of mouse visual cortex. In *bioRxiv* (p. 2021.07.28.454025). https://doi.org/10.1101/2021.07.28.454025

Morrison, M. S., Wang, T., Raguram, A., Hemez, C., & Liu, D. R. (2021). Disulfide-compatible phage-assisted continuous evolution in the periplasmic space. *Nature Communications*, *12*(1), 5959.

M'Saad, O., Kasula, R., Kondratiuk, I., Kidd, P., Falahati, H., Gentile, J. E., Niescier, R. F., Watters, K., Sterner, R. C., Lee, S., Liu, X., De Camilli, P., Rothman, J. E., Koleske, A. J., Biederer, T., & Bewersdorf, J. (2022). All-optical visualization of specific molecules in the ultrastructural context of brain tissue. In *bioRxiv*. https://doi.org/10.1101/2022.04.04.486901

Neuroglancer Documentation. (n.d.). Connectomics with PyTorch. https://connectomics.readthedocs.io/en/latest/external/neuroglancer.html

Nissim, A., Hoogenboom, H. R., Tomlinson, I. M., Flynn, G., Midgley, C., Lane, D., & Winter, G. (1994). Antibody fragments from a 'single pot' phage display library as immunochemical reagents. *The EMBO Journal*, *13*(3), 692–698.

Nusser, Z., Sieghart, W., & Somogyi, P. (1998). Segregation of different GABAA receptors to synaptic and extrasynaptic membranes of cerebellar granule cells. *The Journal of Neuroscience: The Official Journal of the Society for Neuroscience*, *18*(5), 1693–1703.

Pachitariu, M., & Stringer, C. (2022). Cellpose 2.0: how to train your own model. *Nature Methods*, *19*(12),

1634–1641.

Palay, S. L., & Chan-Palay, V. (2012). *Cerebellar Cortex: Cytology and Organization*. Springer Science & Business Media.

Pavarino, E. C., Yang, E., Dhanyasi, N., Wang, M., Bidel, F., Lu, X., Yang, F., Park, C. F., Br, M., Drescher, B., Samuel, A. D. T., Hochner, B., Katz, P. S., Zhen, M., Lichtman, J. W., & Meirovitch, Y. (2023). mEMbrain: an interactive deep learning MATLAB tool for connectomic segmentation on commodity desktops. In *bioRxiv*. https://doi.org/10.1101/2023.04.17.537196

Perez-Witzke, D., Nunez de Villavicencio Diaz, T., Moore, N., Le Bihan, T., Hutchings, N., Sapkota, R., Mobley, M., Xie, M., Ma, B., & Fiebig, M. (n.d.). *Sequencing and Recombinant Expression of Goat Antibodies from a Polyclonal Mixture*. Rapid Novor. https://www.rapidnovor.com/sequencing-recombinant-goat-polyclonal-antibodies/

Rakhymzhan, A., Acs, A., Hauser, A. E., Winkler, T. H., & Niesner, R. A. (2021). Improvement of the Similarity Spectral Unmixing Approach for Multiplexed Two-Photon Imaging by Linear Dimension Reduction of the Mixing Matrix. *International Journal of Molecular Sciences*, *22*(11). https://doi.org/10.3390/ijms22116046

Richards, J. G., Schoch, P., Häring, P., Takacs, B., & Möhler, H. (1987). Resolving GABAA/benzodiazepine receptors: cellular and subcellular localization in the CNS with monoclonal antibodies. *The Journal of Neuroscience: The Official Journal of the Society for Neuroscience*, *7*(6), 1866–1886.

Schmidt, H., Arendt, O., Brown, E. B., Schwaller, B., & Eilers, J. (2007). Parvalbumin is freely mobile in axons, somata and nuclei of cerebellar Purkinje neurones. *Journal of Neurochemistry*, *100*(3), 727–735.

Scotti, A. L., & Nitsch, C. (1992). Differential Ca2+ binding properties in the human cerebellar cortex: distribution of parvalbumin and calbindin D-28k immunoreactivity. *Anatomy and Embryology*, *185*(2), 163–167.

Sen, K. I., Tang, W. H., Nayak, S., Kil, Y. J., Bern, M., Ozoglu, B., Ueberheide, B., Davis, D., & Becker, C. (2017). Automated Antibody De Novo Sequencing and Its Utility in Biopharmaceutical Discovery. *Journal of the American Society for Mass Spectrometry*, *28*(5), 803–810.

Seo, J., Sim, Y., Kim, J., Kim, H., Cho, I., Nam, H., Yoon, Y.-G., & Chang, J.-B. (2022). PICASSO allows ultra-multiplexed fluorescence imaging of spatially overlapping proteins without reference spectra measurements. *Nature Communications*, *13*(1), 2475.

Shapson-Coe, A., Januszewski, M., Berger, D. R., Pope, A., Wu, Y., Blakely, T., Schalek, R. L., Li, P. H., Wang, S., Maitin-Shepard, J., Karlupia, N., Dorkenwald, S., Sjostedt, E., Leavitt, L., Lee, D., Bailey, L., Fitzmaurice, A., Kar, R., Field, B., … Lichtman, J. W. (2021). A connectomic study of a petascale fragment of human cerebral cortex. In *bioRxiv* (p. 2021.05.29.446289). https://doi.org/10.1101/2021.05.29.446289

Shu, X., Lev-Ram, V., Deerinck, T. J., Qi, Y., Ramko, E. B., Davidson, M. W., Jin, Y., Ellisman, M. H., & Tsien, R. Y. (2011). A genetically encoded tag for correlated light and electron microscopy of intact cells, tissues, and organisms. *PLoS Biology*, *9*(4), e1001041.

Stringer, C., Wang, T., Michaelos, M., & Pachitariu, M. (2021). Cellpose: a generalist algorithm for cellular segmentation. *Nature Methods*, *18*(1), 100–106.

Trimmer, J. S. (2015). Subcellular localization of K+ channels in mammalian brain neurons: remarkable precision in the midst of extraordinary complexity. *Neuron*, *85*(2), 238–256.

Trimmer, J. S. (2020). Recombinant Antibodies in Basic Neuroscience Research. *Current Protocols in Neuroscience / Editorial Board, Jacqueline N. Crawley ... [et Al.]*, *94*(1), e106.

UC Davis/NIH NeuroMab Facility. (n.d.). UC Davis/NIH NeuroMab Facility. https://neuromab.ucdavis.edu/neuromabs.cfm

Vishwanathan, A., Daie, K., Ramirez, A. D., Lichtman, J. W., Aksay, E. R. F., & Seung, H. S. (2017). Electron Microscopic Reconstruction of Functionally Identified Cells in a Neural Integrator. *Current Biology: CB*, *27*(14), 2137-2147.e3.

Wei, D., Lin, Z., Franco-Barranco, D., Wendt, N., Liu, X., Yin, W., Huang, X., Gupta, A., Jang, W.-D., Wang, X., Arganda-Carreras, I., Lichtman, J. W., & Pfister, H. (2020). MitoEM Dataset: Large-scale 3D Mitochondria Instance Segmentation from EM Images. *Medical Image Computing and Computer-Assisted Intervention: MICCAI ... International Conference on Medical Image Computing and Computer-Assisted Intervention*, *12265*, 66–76.

Wei, L., Chen, Z., Shi, L., Long, R., Anzalone, A. V., Zhang, L., Hu, F., Yuste, R., Cornish, V. W., & Min, W. (2017). Super-multiplex vibrational imaging. *Nature*, *544*(7651), 465–470.

White, B. M., Kumar, P., Conwell, A. N., Wu, K., & Baskin, J. M. (2022). Lipid Expansion Microscopy. *Journal of the American Chemical Society*, *144*(40), 18212–18217.

Yusakul, G., Sakamoto, S., Pongkitwitoon, B., Tanaka, H., & Morimoto, S. (2016). Effect of linker length between variable domains of single chain variable fragment antibody against daidzin on its reactivity. *Bioscience, Biotechnology, and Biochemistry*, *80*(7), 1306–1312.

Zhang, Q., Lee, W.-C. A., Paul, D. L., & Ginty, D. D. (2019). Multiplexed peroxidase-based electron microscopy labeling enables simultaneous visualization of multiple cell types. *Nature Neuroscience*, *22*(5), 828–839.

Zimmermann, T., Marrison, J., Hogg, K., & O'Toole, P. (2014). Clearing up the signal: spectral imaging and linear unmixing in fluorescence microscopy. *Methods in Molecular Biology* , *1075*, 129–148.

Zuiderveld, K. (1994). Contrast limited adaptive histogram equalization. *Graphics Gems*, *0*, 474–485.